Coupled hydro-mechanical model for partially saturated soils predicting small strain stiffness

Kwong Soon Wong[1,2] and David Mašín[1]

[1] *Charles University in Prague, Faculty of Science, Albertov 6, 12843 Prague 2, Czech Republic*

[2] *Curtin University, Sarawak Campus, CDT 250, 98009, Miri, Sarawak, Malaysia*

correspondence to:

David Mašín

Charles University in Prague

Faculty of Science

Albertov 6

12843 Prague 2, Czech Republic

E-mail: masin@natur.cuni.cz

Tel: +420-2-2195 1552, Fax: +420-2-2195 1556

June 10, 2014

Revised manuscript submitted to the journal

Computers and Geotechnics

Abstract

In the paper, we present newly developed hydro-mechanical hypoplastic model for partially saturated soils predicting small strain stiffness. Hysteretic void ratio dependent water retention model has been incorporated into the existing hypoplastic model. This required thorough revision of the model structure to allow for the hydro-mechanical coupling dependencies. The model is fromulated in terms of degree of saturation, rather than of suction. Subsequently, the small strain stiffness effects were incorporated using the intergranular strain concept modified for unsaturated conditions. New features included degree of saturation-dependent size of the elastic range and an updated evolution equation for the intergranular strain. The model has been evaluated using two comprehensive data sets on completely decomposed tuff from Hong-Kong and Zenos Kaolin from Iran. It has been shown that the modified intergranular strain formulation coupled with the hysteretic water retention model correctly reproduces the effects of both the stress and suction histories on small strain stiffness evolution. The model can correctly predict also different other aspects of partially saturated soil behaviour, starting from the very small strain range up to the asymptotic large-strain response.

Keywords: Partial saturation; hydro-mechanical coupling; hypoplasticity; small strain stiffness; degree of saturation.

1 Introduction

Stiffness at small strains (0.001% to 1%) is a key parameter for predicting ground deformations and dynamic responses of many earth structures such as retaining walls, foundations and tunnels. Moreover, correct consideration of stiffness development is crucial for capturing cyclic loading phenomena, induced for example by environmental effects during wetting and drying cycles. Over the decades, a number of constitutive models have been developed and validated for modelling small strain stiffness in saturated soils [44, 39, 10, 16]. Also, a number of models for predicting very small strain (less than 0.001%) shear modulus of partially saturated soils and its dependency on net stress, suction and void ratio has been developed [37, 42, 3, 20, 45, 48]. Recently, different authors proposed coupled hydro-mechanical constitutive models for partially saturated soils [17, 8, 29, 46, 12, 34, 13, 22, 11, 23]. None of these models, however, predict small strain stiffness behaviour.

From the above summary it is clear that not much research attention has been payed to the stiffness development of partially saturated soils in the small strain range. In fact, to the author's knowledge, no constitutive model capable of predicting the effect of complex phenomena taking place in partially saturated soils on the stiffness evolution in the small strain range has yet been developed.

Such a model is proposed in this paper. The model inherits some features from the earlier hypoplastic models. In addition, it incorporates very small strain stiffness, stiffness evolution in the small strain range and their dependency on stress and suction history and hysteretic water retention curve. The resultant model is comprehensive and it predicts majority of phenomena needed for correct predictions of engineering problems in partially saturated soils with the exception of the following three: effect of temperature, highly swelling behaviour of certain active clays and viscous effects such as creep, relaxation and rate dependence. For their predictions using hypoplastic models the readers are referred to [32, 29, 38].

2 Model formulation

Model formulation is presented in this section. Hypoplastic model presented in this paper has been developed using hierarchical approach on the basis of earlier hypoplastic models. Due to the space reasons, we cannot describe complete model structure within this paper. For this reason, we describe only those features of the model which are novel with respect to the earlier formulations. Summary of the relevant literature sources is given in Table 1. Complete formulation of the model sufficient for its implementation into a numerical code is given in Appendix.

Before incorporating the very small strain stiffness effects, we first need to formulate the underlining hypoplastic model capable of predicting large strain behaviour and asymptotic states. The model is an evolution of the mechanical hypoplastic model for unsaturated soils by Mašín and Khalili [31] and water retention model by Mašín [25]. These models were evaluated by D'Onza et al. [9], demonstrating their good predictive capabilities. The models have been evolved in two ways. First, the new formulation is based on a hypoplastic formulation by Mašín [28, 27], enabling to explicitly incorporate the asymptotic states [26, 15]. The explicit formulation leads to more freedom in further model enhancements (such as the incorporation of stiffness anisotropy, see Mašín and Rott [33]). Second, a hysteretic water retention model is incorporated. This water retention model is described in Sec. 2.1 and its incorporation into hypoplasticity in Sec. 2.2. Sec. 2.3 summarises the recently developed model for the very small strain shear modulus of unsaturated soils by Wong et al. [48]. Finally, its incorporation into hypoplasticity is described in Sec. 2.4.

Different components of the proposed model (position of normal compression lines, very small strain shear modulus, size of the small-strain stiffness elastic range, effective stress) are defined in terms of degree of saturation S_r, rather than in terms of suction s. Similar approach has already been proposed by Zhou et al. [50] and Lloret-Cabot et al. [24].

2.1 Hysteretic water retention model

The water retention model is schematised in Fig. 1. Hysteretic water retention curve formulations have already been proposed by different authors [50, 17, 47, 21, 41, 40, 23]. The model adopted in this paper is based on a non-hysteretic model by Mašín [25], in which the main drying portion of the water retention curve is represented by the Brooks and Corey [5] formulation

$$S_r = \begin{cases} 1 & \text{for} \quad s < s_{en} \\ \left(\frac{s_{en}}{s}\right)^{\lambda_p} & \text{for} \quad s \geq s_{en} \end{cases} \tag{1}$$

where λ_p is the slope of the water retention curve and s_{en} represents the air entry value of suction for the main drying process. The values of s_{en} and λ_p depend on void ratio. The void ratio dependencies of s_{en} and λ_p are calculated by

$$\dot{s}_{en} = -\frac{\gamma s_{en}}{e\lambda_{psu}}\dot{e} \tag{2}$$

with

$$\lambda_{psu} = \frac{\gamma}{\ln \chi_{0su}} \ln\left[\left(\chi_{0su}^{\frac{\lambda_{p0}}{\gamma}} - \chi_{0su}\right)\left(\frac{e}{e_0}\right)^{(\gamma-1)} + \chi_{0su}\right] \tag{3}$$

where $\chi_{0su} = (s_{en0}/s_{en})^{\gamma}$. s_{en0} and λ_{p0} are values of s_{en} and λ_p corresponding to the reference void ratio e_0 (s_{en0}, e_0 and λ_{p0} are model parameters). The dependency of λ_p on void ratio and suction is then given by

$$\lambda_p = \frac{\gamma}{\ln \chi_0} \ln\left[\left(\chi_0^{\frac{\lambda_{p0}}{\gamma}} - \chi_0\right)\left(\frac{e}{e_0}\right)^{(\gamma-1)} + \chi_0\right] \tag{4}$$

with $\chi_0 = (s_{en0}/s)^{\gamma}$.

[Figure 1 about here.]

In the water retention model formulation, the hysteretic nature of water retention curve is controlled by a parameter a_e, which defines the ratio of air expulsion and air entry values of suction (see Fig. 1). The scanning curve formulation is based on a new state variable denoted as a_{scan}, which is defined as

$$a_{scan} = \frac{s - s_W}{s_D - s_W} \tag{5}$$

In Eq. (5), s_D is suction at the main drying curve and s_W at the main wetting curve corresponding to the current degree of saturation S_r (Fig. 1). It follows from (5) and a_e

definition that s_D may be expressed as

$$s_D = \frac{s_{en}}{s_e} s \tag{6}$$

with

$$s_e = s_{en} \left(a_e + a_{scan} - a_e a_{scan} \right) \tag{7}$$

The hysteretic model can then be defined using the rate equation for a_{scan}, such that for $s > a_e s_{en}$

$$\dot{a}_{scan} = \frac{1 - r_\lambda}{s_D(1 - a_e)} \dot{s} \tag{8}$$

where the ratio r_λ is defined as

$$r_\lambda = \begin{cases} 1 & \text{for} \quad s = s_D \quad \text{and} \quad \dot{s} > 0 \\ 1 & \text{for} \quad s = a_e s_D \quad \text{and} \quad \dot{s} < 0 \\ \frac{\lambda_{pscan}}{\lambda_p} & \text{otherwise} \end{cases} \tag{9}$$

The variables λ_p and λ_{pscan} denote the slopes of the main wetting-drying and scanning curves respectively (see Fig. 1). If $s \leq a_e s_{en}$, then $a_{scan} = 0$. Note that $\partial a_{scan}/\partial e = 0$ is assumed. Thus, the position along scanning curve does not influence the dependency of S_r on void ratio. Finite expression for S_r of the hysteretic model then reads simply:

$$S_r = \begin{cases} 1 & \text{for} \quad s \leq a_e s_{en} \\ \left(\frac{s_e}{s} \right)^{\lambda_p} & \text{for} \quad s > a_e s_{en} \end{cases} \tag{10}$$

Note that different model components described in the next paragraphs are defined using the ratio s_e/s (for $s > s_e$). There is a direct relationship between s_e/s and S_r (from (10)):

$$\frac{s_e}{s} = S_r^{(1/\lambda_p)} \tag{11}$$

The model is thus primarily defined in terms of degree of saturation.

2.2 Incorporation of hysteretic void ratio dependent water retention model into hypoplasticity

Modifications of the basic hypoplastic model by Mašín and Khalili [31] are needed to incorporate hysteretic void-ratio dependent water retention curve. The general rate equation of the model reads:

$$\mathring{\boldsymbol{\sigma}} = f_s \left(\boldsymbol{\mathcal{L}} : \dot{\boldsymbol{\epsilon}} + f_d \mathbf{N} \|\dot{\boldsymbol{\epsilon}}\| \right) + f_u \mathbf{H}_s \tag{12}$$

where $\boldsymbol{\mathcal{L}}$ and $\mathbf{N}$ are fourth- and second-order constitutive tensors respectively, $\dot{\boldsymbol{\epsilon}}$ is the Euler stretching tensor, $\|\dot{\boldsymbol{\epsilon}}\|$ is the Euclidean norm of $\dot{\boldsymbol{\epsilon}}$, $\mathbf{H}$ is the second-order tensor enabling to predict wetting-induced collapse and the circle symbol ($\mathring{\boldsymbol{\sigma}}$) denotes objective (Jaumann) rate. The other factors are defined in Appendix and references from Table 1.

To incorporate hysteretic water retention model, we need to consider the dependency of the effective stress on void ratio. The model is based on the effective stress approach. Throughout the past, a number of effective stress formulations have been developed and discussed by different researchers [4, 14, 7, 18, 19]. In this work, an expression by Khalili and Khabbaz [18] is considered with:

$$\boldsymbol{\sigma} = \boldsymbol{\sigma}^{net} - \mathbf{1}\chi s \tag{13}$$

Where $\boldsymbol{\sigma}^{net}$ is net stress and s represents suction. For $S_r < 1$

$$\chi = \left(\frac{s_e}{s}\right)^{\gamma} \tag{14}$$

and $\chi = 1$ otherwise. Eq. (13) can also be expressed for the adopted water retention model as

$$\chi = S_r^{(\gamma/\lambda_p)} \tag{15}$$

(see [9]). The expression (15) is consistent with the model by Alonso et al. [1], who proposed $\chi = S_r^{\alpha}$ with a parameter $\alpha \geq 1$. It may not properly behave along hydraulic scanning paths, however, as indicated by Khalili and Zargarbashi [19]. Unlike in the original model, in which s_e is considered to be material constant independent of e, the effective stress rate equation of the new model reads

$$\mathring{\boldsymbol{\sigma}} = \mathring{\boldsymbol{\sigma}}^{net} - \mathbf{1}\frac{\partial(\chi s)}{\partial t} = \mathring{\boldsymbol{\sigma}}^{net} - \mathbf{1}\left[\frac{\partial(\chi s)}{\partial s}\dot{s} + \frac{\partial(\chi s)}{\partial e}\dot{e}\right] \tag{16}$$

The derivative $\partial\chi s/\partial s$ in the hysteretic water retention curve formulation can be expressed using variable r_λ defined in Eq. (9) as

$$\frac{\partial(\chi s)}{\partial s} = (1 - \gamma r_\lambda)\,\chi \tag{17}$$

Eq. (17) follows from (14), and its derivation takes into account that s_e changes with suction when the state moves along hydraulic scanning curve. The derivative $\partial(\chi s)/\partial e$ then follows from the Mašín [25] model, that is from Eq. (2). Equations (1) and (2) yield for $s > s_e$

$$\frac{\partial(\chi s)}{\partial e} = -\frac{s\gamma^2}{e\lambda_{psu}}\left(\frac{s_{en}}{s}\right)^{\gamma} \tag{18}$$

and $\partial(\chi s)/\partial e = 0$ otherwise.

Eq. (18) can be incorporated into the model rate formulation by transferring the $\partial(\chi s)/\partial e$ term to the right-hand side of the hypoplastic equation. For $S_r < 1$ (for $s > s_e$)

$$\overset{\circ}{\boldsymbol{\sigma}}^{net} - \mathbf{1}\left(1 - \gamma r_\lambda\right)\chi\dot{s} = f_s\left(\boldsymbol{\mathcal{L}}^{HM} : \dot{\boldsymbol{\epsilon}} + f_d \mathbf{N}\|\dot{\boldsymbol{\epsilon}}\|\right) + f_u \mathbf{H}_s \tag{19}$$

where

$$\boldsymbol{\mathcal{L}}^{HM} = \boldsymbol{\mathcal{L}} - \frac{s(1+e)\gamma^2}{f_s e \lambda_{psu}}\left(\frac{s_{en}}{s}\right)^{\gamma} \mathbf{1} \otimes \mathbf{1} \tag{20}$$

and for $S_r = 1$ (for $s < s_e$):

$$\overset{\circ}{\boldsymbol{\sigma}}^{net} - \mathbf{1}\dot{s} = f_s\left(\boldsymbol{\mathcal{L}} : \dot{\boldsymbol{\epsilon}} + f_d \mathbf{N}\|\dot{\boldsymbol{\epsilon}}\|\right) \tag{21}$$

At this point, it is possible to calculate the $\mathbf{H}_s$ term. For its evaluation, we need to define the dependency of normal compression line on suction and on s_e. We adopt the following formulation, linear in the $\ln(1+e)$ vs. $\ln p$ plane [6], which has already been adopted in the Mašín and Khalili [31] model.

$$\ln(1+e) = N(s) - \lambda^*(s) \ln \frac{p}{p_r} \tag{22}$$

where variables $N(s)$ and $\lambda^*(s)$ and parameters n_s and l_s are defined using

$$N(s) = N + n_s \left\langle \ln\left(\frac{s}{s_e}\right)\right\rangle \qquad \lambda^*(s) = \lambda^* + l_s \left\langle \ln\left(\frac{s}{s_e}\right)\right\rangle \tag{23}$$

where N, λ^*, l_s and n_s are model parameters. Mašín and Khalili [31] derived the following general expression of the $\mathbf{H}_s$ term:

$$\mathbf{H}_s = -\frac{\boldsymbol{\sigma}}{p_e}\frac{\partial p_e}{\partial s}\langle -\dot{s}\rangle \tag{24}$$

where p_e is Hvorslev equivalent pressure, that is mean effective stress at the normal compression line at the current value of suction and void ratio. p_e is calculated from the normal compression line formulation (22). When deriving a formulation for $\mathbf{H}_s$ using (24), we need to take into account that p_e depends on s directly through the dependency of $N(s)$ and $\lambda^*(s)$ on s, and also through the dependency of s_e on s when the state is at the hydraulic scanning curve. After some algebra it turns out that

$$\mathbf{H}_s = -\frac{c_i r_\lambda \boldsymbol{\sigma}}{s\lambda^*(s)}\left(n_s - l_s \ln \frac{p_e}{p_r}\right)\langle -\dot{s}\rangle \tag{25}$$

The factor c_i has been introduced in [32] to enhance the model performance in overconsolidated states and it is specified later in the text.

The last modification of the model reflects variability of s_e with void ratio. As the slope $\lambda^*(s)$ and intercept N of normal compression line depends on s/s_e, variability of s_e during loading process causes that the actual slope of normal compression line slightly differs from $\lambda^*(s)$. The actual slope of normal compression line λ^*_{act} may be calculated in the following way. Time derivative of the normal compression line formulation (22) accompanied with (23) yields

$$\frac{\dot{e}}{1+e} = -\lambda^*(s)\frac{\dot{p}}{p} - \left(n_s - l_s \ln\frac{p}{p_r}\right)\frac{\dot{s}_e}{s_e} \tag{26}$$

The ratio $\dot{s}_e/s_e$ is for constant suction equal to $\dot{s}_{en}/s_{en}$, thanks to the assumption of $\partial a_{scan}/\partial e = 0$. The dependency of s_{en} on void ratio is given by Eq. (2). It can be combined with (26) leading to

$$\frac{\dot{e}}{1+e}\left[1 - \frac{(1+e)\gamma[n_s - l_s \ln(p/p_r)]}{e\lambda_{psu}}\right] = -\lambda^*(s)\frac{\dot{p}}{p} \tag{27}$$

which can be compared with $\dot{e}/(1+e) = -\lambda_{act}\dot{p}/p$ yielding for $S_r < 1$

$$\lambda^*_{act} = \lambda^*(s)\frac{e\lambda_{psu}}{e\lambda_{psu} - \gamma(1+e)[n_s - l_s \ln(p/p_r)]} \tag{28}$$

$\lambda^*_{act} = \lambda^*$ for $S_r = 1$. To ensure consistent predictions of the model with the modified compression law (and thus to ensure the state does not drift from the state boundary surface during asymptotic loading), λ^*_{act} enters the expression of the hypoplastic tensor $\boldsymbol{\mathcal{A}}$, barotropy factor f_s and scalar multiplier c_i. For their definition see Appendix. It follows that

$$\boldsymbol{\mathcal{A}} = f_s\boldsymbol{\mathcal{L}} + \frac{\boldsymbol{\sigma}}{\lambda^*_{act}} \otimes \mathbf{1} \tag{29}$$

$$f_s = -\frac{3\,\mathrm{tr}\,\boldsymbol{\sigma}}{2A_m}\left(\frac{1}{\lambda^*_{act}} + \frac{1}{\kappa^*}\right) \tag{30}$$

$$c_i = \frac{(\lambda^*_{act} + \kappa^*)\left(2^{\alpha_f} - f_d\right) + 2\kappa^* f_d}{(\lambda^*_{act} + \kappa^*)\left(2^{\alpha_f} - f_d^A\right) + 2\kappa^* f_d^A} \tag{31}$$

The factor $\mathbf{H}_s$ is calculated using the value of $\lambda^*(s)$ to predict correctly the wetting-induced collapse.

2.3 Formulation for the very small strain shear modulus

Incorporation of small strain stiffness and its evolution into a constitutive model requires three main components: a model for large strain response, reference value of the very small strain stiffness and a model describing the stiffness degradation at small strains. The first component has been discussed in Sec. 2.2 and the last one will be described in Sec. 2.4. In this section, we describe the adopted formulation for the very small strain shear modulus

G_{tp0}. The formulation has been developed by Wong et al. [48] and it reads:

$$G_{tp0} = p_r A_g \left(\frac{p}{p_r}\right)^{n_g} e^{(-m_g)} S_r^{(-k_g/\lambda_p)} \tag{32}$$

$$G_{tp0} = p_r A_g \left(\frac{p}{p_r}\right)^{n_g} e^{(-m_g)} \left(\frac{s}{s_e}\right)^{k_g} \tag{33}$$

where p is mean effective stress calculated using χ factor of Eq. (14). In Eq. (32), p_r is a reference pressure of 1 kPa. A_g, n_g, m_g and k_g are model parameters controlling G_{tp0} magnitude and its dependency on mean effective stress, void ratio and degree of saturation. It is pointed out that the dependency of G_{tp0} on mean stress, void ratio and S_r from Eq. (32) violates the principle of conservation of energy [52].

The Equation (32) predicts both the effects on G_{tp0} of mechanical hysteresis (thanks to the void ratio term) and of hydraulic hysteresis (thanks to the S_r term combined with the hysteretic water retention curve formulation). Example evaluation of the model will be shown in Sec. 4, more details can be found in Wong et al. [48].

2.4 Hypoplastic model incorporating small strain stiffness

Small strain stiffness effects have been incorporated by means of the intergranular strain concept proposed by Niemunis and Herle [39]. In this paper, we describe a modification of this concept for partially saturated conditions. In addition, we adopt transversely elastic small strain stiffness model formulation, developed by Mašín and Rott [33] and incorporated into saturated hypoplastic model by Mašín [30].

In the extended hypoplastic model the strain is considered as a result of deformation of the intergranular interface layer and of rearrangement of the skeleton Niemunis and Herle [39]. The interface deformation is called *intergranular strain* $\boldsymbol{\delta}$ and is considered as a tensorial state variable. It is convenient to denote the normalized magnitude of $\boldsymbol{\delta}$ as

$$\rho = \frac{\|\boldsymbol{\delta}\|}{R(s)} \tag{34}$$

where $R(s)$ represents size of the elastic range. The direction $\hat{\boldsymbol{\delta}}$ of the intergranular strain is defined as

$$\hat{\boldsymbol{\delta}} = \begin{cases} \boldsymbol{\delta}/\|\boldsymbol{\delta}\| & \text{for } \boldsymbol{\delta} \neq \mathbf{0} \\ \mathbf{0} & \text{for } \boldsymbol{\delta} = \mathbf{0} \end{cases} \tag{35}$$

The general stress–strain relation is now written as

$$\mathring{\boldsymbol{\sigma}} = \boldsymbol{\mathcal{M}} : \dot{\boldsymbol{\epsilon}} + f_u \mathbf{H}_s \tag{36}$$

The fourth-order tensor $\boldsymbol{\mathcal{M}}$ represents stiffness and is calculated from the hypoplastic tensors $\boldsymbol{\mathcal{L}}$ and $\mathbf{N}$ using the following interpolation:

$$\boldsymbol{\mathcal{M}} = \left[\rho^{\chi_g} m_T + (1-\rho^{\chi_g})\, m_R\right] f_s \boldsymbol{\mathcal{L}} + \begin{cases} \rho^{\chi_g}\,(1-m_T)\, f_s \boldsymbol{\mathcal{L}} : \hat{\boldsymbol{\delta}} \otimes \hat{\boldsymbol{\delta}} + \rho^{\chi_g} f_s f_d \mathbf{N} \hat{\boldsymbol{\delta}} & \text{for } \hat{\boldsymbol{\delta}} : \dot{\boldsymbol{\epsilon}} > 0 \\ \rho^{\chi_g}\,(m_R - m_T)\, f_s \boldsymbol{\mathcal{L}} : \hat{\boldsymbol{\delta}} \otimes \hat{\boldsymbol{\delta}} & \text{for } \hat{\boldsymbol{\delta}} : \dot{\boldsymbol{\epsilon}} \leq 0 \end{cases} \tag{37}$$

From the mathematical standpoint, the above expression implies interpolation between the following three special cases:

$$\begin{array}{lll} \mathring{\boldsymbol{\sigma}} = m_R f_s \boldsymbol{\mathcal{L}} : \dot{\boldsymbol{\epsilon}} & \text{for} & \hat{\boldsymbol{\delta}} : \dot{\boldsymbol{\epsilon}} = -1 \text{ or } \boldsymbol{\delta} = \mathbf{0} \\ \mathring{\boldsymbol{\sigma}} = m_T f_s \boldsymbol{\mathcal{L}} : \dot{\boldsymbol{\epsilon}} & \text{for} & \hat{\boldsymbol{\delta}} : \dot{\boldsymbol{\epsilon}} = 0 \text{ and } \boldsymbol{\delta} \neq \mathbf{0} \\ \mathring{\boldsymbol{\sigma}} = f_s \boldsymbol{\mathcal{L}} : \dot{\boldsymbol{\epsilon}} + f_s f_d \mathbf{N} \|\dot{\boldsymbol{\epsilon}}\| & \text{for} & \hat{\boldsymbol{\delta}} : \dot{\boldsymbol{\epsilon}} = 1 \end{array} \tag{38}$$

It thus follows that the variable m_R controls stiffness magnitude in the very small strain range. In the original model, m_R served as a parameter. In the new model, m_R is a variable controlling very small strain stiffness magnitude. It is calculated to ensure the very small strain shear modulus is expressed using Eq. (32). The shear modulus component of the tensor $m_R f_s \boldsymbol{\mathcal{L}}$ reads [30]

$$G_{0tp} = m_R \frac{9p}{2A_m} \left(\frac{1}{\lambda^*} + \frac{1}{\kappa^*} \right) \frac{\alpha_E}{2\alpha_G} \left(1 - \nu_{pp} - 2\frac{\alpha_E}{\alpha_\nu^2} \nu_{pp}^2 \right) \tag{39}$$

The present model incorporates stiffness anisotropy, the subscripts $_t$ and $_p$ in (39) refer to the transversal and in-plane direction respectively with respect to the plane of transversal isotropy. For more details see [33, 30]. Different variables from (39) are described in Appendix. By considering that $G_{0tp} = G_{tp0}$ it follows that

$$m_R = G_{tp0} \frac{4A_m \alpha_G}{9p\alpha_E} \left(\frac{\lambda^*_{act} \kappa^*}{\lambda^*_{act} + \kappa^*} \right) \frac{1}{1 - \nu_{pp} - 2\frac{\alpha_E}{\alpha_\nu^2} \nu_{pp}^2} \tag{40}$$

where G_{tp0} is defined in Eq. (32).In the modified model, parameter m_{rat} is adopted instead of the original parameter m_T, such that

$$m_T = m_{rat} m_R \tag{41}$$

The size of the elastic range is in the original intergranular strain model defined by the parameter R. Evaluation of the model using experimental data on small strain stiffness of partially saturated soils revealed that the size of the elastic range depends on the current value of the ratio s/s_e (that is, it depends on current degree of saturation). We can recall similarity with the behaviour of cemented soils. As observed, among others, by Sharma and

Fahey [43], the amount of cementing agent increases the size of the elastic range. In the small strain stiffness hypoplastic model, the size of the elastic range, denoted as $R(s)$, is calculated as

$$R(s) = R + r_m \ln \frac{s}{s_e} = R - \frac{r_m}{\lambda_p} \ln S_r \tag{42}$$

where r_m is a model parameter controlling the dependency of $R(s)$ on the ratio s/s_e (and thus on S_r). Parameter r_m can be calibrated using stiffness degradation curves at different suction levels.

The evolution of the intergranular strain tensor $\boldsymbol{\delta}$ is in the original model governed by

$$\mathring{\boldsymbol{\delta}} = \begin{cases} \left(\boldsymbol{\mathcal{I}} - \hat{\boldsymbol{\delta}} \otimes \hat{\boldsymbol{\delta}} \rho^{\beta_r}\right) : \dot{\boldsymbol{\epsilon}} & \text{for } \hat{\boldsymbol{\delta}} : \dot{\boldsymbol{\epsilon}} > 0 \\ \dot{\boldsymbol{\epsilon}} & \text{for } \hat{\boldsymbol{\delta}} : \dot{\boldsymbol{\epsilon}} \leq 0 \end{cases} \tag{43}$$

where $\mathring{\boldsymbol{\delta}}$ is the objective rate of intergranular strain. In the new formulation, $R(s)$ depends on both suction and void ratio. Time derivative of (42) yields

$$\dot{R}(s) = r_m \left(r_\lambda \frac{\dot{s}}{s} + \frac{\gamma}{e \lambda_{psu}} \dot{e} \right) \tag{44}$$

where λ_{psu} is a variable specified in the model from [25]. To consider the fact that suction and void ratio influence the size of the elastic range, rate formulation of the intergranular strain is adjusted such that for $\hat{\boldsymbol{\delta}} : \dot{\boldsymbol{\epsilon}} > 0$, $s > s_e$ and $\dot{R}(s) < 0$

$$\mathring{\boldsymbol{\delta}} = \left(\boldsymbol{\mathcal{I}} - \hat{\boldsymbol{\delta}} \otimes \hat{\boldsymbol{\delta}} \rho^{\beta_r}\right) : \dot{\boldsymbol{\epsilon}} + \boldsymbol{\delta} \frac{\dot{R}(s)}{R(s)} \tag{45}$$

For other cases, the original formulation remains unchanged. Eq. (45) ensures the Euclidean norm of the intergranular strain tensor $\|\boldsymbol{\delta}\|$ never exceeds $R(s)$ (such a state would physically be inadmissible). $R(s)$ variation does not affect the intergranular strain direction $\hat{\boldsymbol{\delta}}$. Note that Eq. (45) considers the effect of both recent stress and suction history on the intergranular strain evolution, as both both stress and suction variation imply soil deformation, which in turn imply change of $\boldsymbol{\delta}$.

The integration of the enhanced model may be utilised in the same way as the integration of the basic hysteretic model in Sec. 2.2. That is, the $\partial(\chi s)/\partial e$ term can be transferred to the right-hand side of the hypoplastic equation such that for $S_r < 1$ (for $s > s_e$)

$$\mathring{\boldsymbol{\sigma}}^{net} - \mathbf{1}\left(1 - \gamma r_\lambda\right) \chi \dot{s} = \boldsymbol{\mathcal{M}}^{HM} : \dot{\boldsymbol{\epsilon}} + f_u \mathbf{H}_s \tag{46}$$

where

$$\boldsymbol{\mathcal{M}}^{HM} = \boldsymbol{\mathcal{M}} - \frac{s(1+e)\gamma^2}{e \lambda_{psu}} \left(\frac{s_{en}}{s}\right)^{\gamma} \mathbf{1} \otimes \mathbf{1} \tag{47}$$

For $S_r = 1$, the original $\boldsymbol{\mathcal{M}}$ is used in the model integration.

3 Model parameters

A complete list of model parameters, together with citations of relevant literature sources where the individual parameter calibration procedures are described, is presented in Table 1.

[Table 1 about here.]

Physical meaning of the individual parameters is as follows:

- φ_c: Parameter of the basic hypoplastic model for saturated clays [28], critical state friction angle.
- λ^*: Parameter of the basic hypoplastic model for saturated clays [28], slope of normal compression line in the $\ln p/p_r$ vs. $\ln(1+e)$ plane where p_r is reference stress 1 kPa.
- N: Parameter of the basic hypoplastic model for saturated clays [28], position of normal compression line in the $\ln p$ vs. $\ln(1+e)$ plane, that is value of $\ln(1+e)$ for $p = p_r$.
- κ^*: Parameter of the basic hypoplastic model for saturated clays [28], controlling unloading-reloading bulk modulus.
- ν_{pp}: Parameter of the basic hypoplastic model for saturated clays [28], controlling stiffness in shear.
- α_G: Parameter of the hypoplastic model with very small strain stiffness anisotropy [33]. α_G represents the ratio of shear modulus within the plane of isotropy G_{pp} and transversal G_{tp}.
- n_s: Parameter of the mechanical hypoplastic model for partially saturated soils [31]. Specifies the dependency of position of normal compression line on S_r (on the ratio s/s_e) within the $\ln p$ vs. $\ln(1+e)$ plane.
- l_s: Parameter of the mechanical hypoplastic model for partially saturated soils [31]. Specifies the dependency of slope of normal compression line on S_r (on the ratio s/s_e) within the $\ln p$ vs. $\ln(1+e)$ plane.
- m: Parameter of the mechanical hypoplastic model for partially saturated soils [31]. Specifies how the wetting-induced collapsible behaviour depends on soil overconsolidation.

- s_{en0}: Parameter of the non-hysteretic water retention model [25]. s_{en0} represents the air-entry value of suction for the reference void ratio e_0.

- λ_{p0}: Parameter of the non-hysteretic water retention model [25]. λ_{p0} represents the slope of water retention curve in the plane of $\ln S_r$ vs. $\ln(s_e/s)$, where s_e is in the present case calculated to reflect water retention curve hysteresis.

- e_0: Parameter of the non-hysteretic water retention model [25]. e_0 represents reference void ratio for s_{en0} and λ_{p0}.

- a_e: Parameter of the hysteretic water retention model from this paper. a_e represents the ratio of the air-expulsion and air-entry value of suction (Fig. 1).

- A_g: Parameter of the very small strain stiffness modulus of partially saturated soils model [48]. A_g presents the value of transversal very small strain shear modulus G_{tp0} of saturated soil for the reference stress $p_r = 1kPa$.

- n_g: Parameter of the very small strain stiffness modulus of partially saturated soils model [48]. n_g controls the dependency of transversal very small strain shear modulus G_{tp0} of saturated soil on mean effective stress p.

- m_g: Parameter of the very small strain stiffness modulus of partially saturated soils model [48]. n_g controls the dependency of transversal very small strain shear modulus G_{tp0} of saturated soil on void ratio.

- k_g: Parameter of the very small strain stiffness modulus of partially saturated soils model [48]. k_g specifies the dependency of transversal very small strain shear modulus G_{tp0} of partially saturated soil on degree of saturation S_r.

- R: Parameter of the intergranular strain concept for small strain stiffness predictions [39]. R represents the size of the very-small-strain elastic range of saturated soil, measured by the Euclidean norm of strain within the strain space.

- β_r: Parameter of the intergranular strain concept for small strain stiffness predictions [39]. β_r controls stiffness decrease in the small strain range.

- χ_g: Parameter of the intergranular strain concept for small strain stiffness predictions [39]. χ_g controls stiffness decrease in the small strain range.

- m_{rat}: Parameter of the intergranular strain concept for small strain stiffness predictions [39]. m_{rat} controls the ratio of very-small-strain shear modulus upon $90°$ change of strain paths direction and upon complete ($180°$) strain path direction reversal.

- r_m: Parameter of the intergranular strain concept for partially saturated soils (this contribution). r_m controls the dependency of the size of the elastic range on degree of saturation.

- γ: Parameter of the effective stress model [18]. A default value of $\gamma = 0.55$ suggested.

4 Evaluation of the model

In this section, the proposed constitutive model is evaluated using experimental data on different soils. Evaluation of the the small strain stiffness characteristics of the model and effects of hydromechanical coupling is being presented comprehensively. Evaluation of predictions of the very small strain stiffness (that is, predictions of the model for G_{tp0}) is just briefly outlined here, as it is out of the main scope of the present paper; the readers are referred to Wong et al. [48] for complete model evaluation.

4.1 Completely decomposed tuff

The first material chosen for evaluation is completely decomposed tuff (CDT) from Hong-Kong. The material tested was extracted from a deep excavation site at Fanling, Hong Kong [37]. The soil would be described as clayey silt (ML) according to the Unified Soil Classification System. The material was yellowish-brown, slightly plastic, with a very small percentage of fine and coarse sand. Specimens were prepared by static compaction at initial water content of about 16.3% and dry density of about 1760 kg/m^3. The average initial suction of the specimens after compaction was 95 kPa. For details on the tested soil, see Ng and Yung [37].

Very small strain shear moduli measurements have been reported by Ng and Yung [37] and Ng et al. [36]. Different types of experiments have been performed and simulated:

1. Isotropic compression tests at constant matric suction. Four different experiments have been performed and simulated, at matric suctions of 0, 50, 100 and 200 kPa. The experimental stress-suction paths are clear from Fig. 2a [37].

2. Drying-wetting tests at the isotropic stress state and constant mean net stress. Two tests with mean net stresses of 110 kPa and 300 kPa have been simulated. Stress paths are shown in Fig. 2b [36].

Very small strain shear stiffness was in [37, 36] measured by bender elements. They measured both G_{tp0} and G_{pp0} using horisontally and vertically mounted bender elements. In the calibration of parameters A_g, m_g, n_g and k_g, G_{tp0} measurements were adopted. The measured anisotropy ratio $\alpha_G = G_{pp0}/G_{tp0}$ was between 1.03 and 1.09. Thus, the anisotropy was insignificant and the value $\alpha_G = 1.0$ was adopted in the simulations.

[Figure 2 about here.]

Experimental measurements of G_{tp0} during the constant suction isotropic compression tests are shown in Fig. 3. The parameters A_g, m_g, n_g and k_g have been calibrated by a trial and error procedure to fit the very small strain stiffness data at $s = 0$, 50 and 100 kPa. Simulations are also included in Fig. 3, revealing that both the dependency of G_{tp0} on mean effective stress and suction has been predicted properly by the model. Model parameters are in Table 2.

[Table 2 about here.]

[Figure 3 about here.]

For model validation, drying-wetting tests at constant net stress have been simulated. Experimental measurements and the G_{tp0} dependency on S_r (on the ratio s/s_e) predicted by the model during wetting-drying tests are shown in Fig. 4. The model represents the hysteretic response. This hysteresis is implied by the hysteretic water retention curve (Fig. 1). Unlike the model, however, the experimental data reveal hysteresis in the suction range below 50 kPa. This is not predicted by the model, due to the inaccurate representation of the wetting branch of water retention curve in the low suction range (see Fig. 6). The model also underpredicts the initial shear modulus measured at $p^{net} = 300$ kPa. This is implied by inconsistency between the data by Ng and Yu [37] (used for model calibration) and Ng et al. [36] (used for model evaluation).

[Figure 4 about here.]

To evaluate the model predictions in the small strain range including the dependency of shear modulus degradation curve on stress and suction history, the experimental data by Ng and Xu [35] and Xu [49] were simulated. They used soil from the same locality as the soil adopted in G_{tp0} measurements. Different samples were, however, used in the two investigations, which implied minor differences in soil properties caused by the soil natural variability.

The following experiments were used in the model evaluation:

1. The first set of experiments has been designed to investigate the effect of suction magnitude on small strain stiffness. The samples were loaded isotropically under constant suction from the as-compacted state of $s = 95$ kPa and $p^{net} = 0$ kPa until the mean

net stress of 100 kPa. Subsequently, suction was increased to either 150 or 300 kPa or decreased to 1 kPa. Then, the samples were sheared under constant p^{net} conditions and stiffness degradation curve was recorded. The stress-suction paths of the three tests are clear from Fig. 5. The three experiments described are represented by pre-shear suction histories $95-1$, $95-150$ and $95-300$. Suctions are indicated in kPa and suction histories are used as test labels in the following text. The initial hydraulic states of the $95-150$ and $95-300$ tests tests are shown in Fig. 6b.

[Figure 5 about here.]

2. The second set of experiments has been designed to investigate the effect of suction history on small strain stiffness. The test $95-150$ described previously has been supplemented by the test $95-300-150$. The shear stage of the two tests has thus been performed at the same suction of $s = 150$ kPa. The immediate past suction history of one test was drying from 95 to 150 kPa, while the history of the other test was wetting from 300 kPa to 150 kPa. This resulted in different initial hydraulic states; the state of one sample being close to the wetting branch of water retention curve, while the state of the other sample being on the drying branch of water retention curve.

3. The third set of experiments is characterised by suction histories $95-300-150$, $95-300-150-180-150$ and $95-300-150-250-150$. Although the suction histories are different in the three cases, the initial hydraulic state is practically the same, as the state of all the three samples is on the wetting branch of water retention curve initially.

4. The fourth set of experiments is characterised by suction histories $95-300-150$, $95-300-150-120-150$ and $95-300-150-90-150$. The initial hydraulic states of the samples are different due to the water retention curve hysteresis (Fig. 6b).

5. The fifth set of experiments has been designed to investigate the effect of mean net stress on stiffness degradation curve. The two samples in this data set had the same suction histories of $95-300-150-50-150$. One was tested at $p^{net} = 100$ kPa, while the other at $p^{net} = 200$ kPa.

To simulated the tests with the proposed model, all the model parameters had to be calibrated first. Detailed description of the calibration procedure is out of the length limits for the present paper; the parameters are summarised in Table 2. Central to the present developments is calibration of water retention curve. Experimental data and model predictions are shown in Fig. 6a. The model represents the basic features of hysteretic hydraulic behaviour, it is however clear that the bi-linear representation is not accurate in the low suction range. Critical state friction angle of $\varphi_c = 35°$ has been taken over from Zhou [51]. In all cases, complete sample stress-suction histories have been simulated, starting from the as-compacted state of $p^{net} = 1$ kPa, $s = 95$ kPa, $e = 0.568$ and $S_r = 0.792$. These values were calculated from the target values reported by Ng and Xu [35] – the optimum water content of 16.3%, dry density of 1760 kg/m^3 and specific gravity of 2.76. The initial value of suction of 95 kPa was the average value of suction of the specimens after compaction as measured by a high-capacity suction probe. The initial value of the vertical component of the intergranular strain was $\delta_{11} = -0.000128$, the other componenets were equal to 0 initially. The initial value of δ_{11} is reflecting the process of sample preparation (one-dimensional static compaction). It was specified such that $\|\boldsymbol{\delta}\| = R(s)$.

[Figure 6 about here.]

[Figure 7 about here.]

Figure 8a shows predictions of G degradation by the model for the first set of experiments. The model represents well the dependency of stiffness degradation curve on the initial suction. Also correctly are predicted curves of normalised shear modulus G/G_{tp0} (Fig. 8b) and deviatoric stress q (Fig. 8c). For comparison purposes, Fig. 8d shows predictions by the model with $r_m = 0$ (that is, with suction-independent size of the elastic range). Predictions are clearly worst than predictions by the model in which the suction-dependent size of the elastic range is considered.

[Figure 8 about here.]

Simulations of the second set of experiments are shown in Fig. 9. The model predicts properly the trend in the dependency of shear stiffness (Fig. 9a) and normalised shear stiffness G/G_{tp0} (Fig. 9b) degradation on suction history. The reason for this model capability may be explained with the aid of Figs. 6b and 7. As soil state of one test is at the main drying branch of water retention curve, while state of the other test is close to the main wetting branch, the two samples are characterised by different values of the ratio s/s_e (although suction is the same in both cases). As s/s_e enters the expression for the elastic range size $R(s)$ (Eq. (42)), the elastic range of the recently wetted sample 95-300-150 is larger than the elastic range of the recently dried sample 95-150.

Fig. 9c shows simulations with $r_m = 0$. While the dependency of $R(s)$ on s/s_e clearly improves predictions (compare 9a and 9c), it is clear that the dependency of $R(s)$ on s/s_e is not the only model feature affecting the results. The two stiffness degradation curves differ even in the case of $r_m = 0$ (constant $R(s)$). The difference in the curves in Fig. 9c is caused by different recent histories, which affect the initial pre-shear value of the intergranular strain tensor. This is clear from Fig. 7, which shows the initial values of the intergranular strain tensor and their evolution during the shear tests for all the simulated tests. Fig. 7b demonstrates that the maximum value of $\|\boldsymbol{\delta}\|$ never exceeds $R(s)$.

[Figure 9 about here.]

Figure 10 shows simulations of the third set of experiments. The samples were subjected to additional drying-wetting cycle. The hydraulic states before and after the additional cycle are in both cases the same (Fig. 6b). The initial values of the intergranular strain are also very similar, although not identical (Fig. 7). As a consequence, the model predicts practically the same stiffness degradation curves. These predictions are in agreement with experimental data.

[Figure 10 about here.]

The fourth set of experiments is simulated in Fig. 11. Now, the test 95-300-150 is supplemented by two tests with additional wetting-drying cycle. The initial states are different due to both the hydraulic (Fig. 6b) and recent strain (Fig. 7) histories. Consequently, the two stiffness degradation curves differ, qualitatively in agreement with the experiment. Simulations with $r_m = 0$ (Fig. 11c) reproduce all similar stiffness degradation curves, indicating that it is the dependency of R on S_r (on the ratio s/s_e) which has major influence on predictions.

[Figure 11 about here.]

Finally, the fifth set of experiments is simulated in Fig. 12. The samples have identical suction histories of $95 - 300 - 50 - 150$, but they are tested at different mean net stresses of 100 and 200 kPa respectively. The different mean net stresses imply different initial shear modulus G_{tp0} predicted correctly by the model (Fig. 12a and Fig. 12c). Due to the same suction histories the normalised stiffness degradation curves practically do not differ in the two cases (Fig. 12b). The experimental data show some influence of p^{net}, however, which is not captured by the model.

[Figure 12 about here.]

4.2 Zenos Kaolin

The second data set used in the model evaluation is on Zenos Kaolin. The experimental results have been published by Biglari et al. [3, 2]. Zenos Kaolin data allow for evaluation of the hydro-mechanical coupling capabilities and G_{tp0} predictions of the model during various stress-suction paths. Unlike CDT described in the previous section, Zenos Kaolin is wetting-induced collapsible soil, and thus also this modelling feature can be evaluated.

Zenos Kaolin is a commercial Iranian kaolin from a mine in northwest Iran. The soil has a clay fraction of about 18% and a silty fraction of about 60%, liquid limit of 29%, plastic limit of 17%. It is classified as lean clay (CL) according to Unified Soil Classification System. The soil samples were prepared by static compaction at a water content of 11.9% (3.5% less than the optimum water content of the standard Proctor compaction test) [2]. Soil was tested under isotropic stress state in suction-controlled resonant column apparatus. Five experiments have been simulated, denoted as C,D,E,F and G. Mean net stress vs. suction paths followed during the tests are shown in Fig. 13 [2]. In all cases, complete sample histories were modelled starting from the as-compacted state of $e = 1.166$, $S_r = 0.27$, $p^{net} = 1$ kPa, $s = 240$ kPa. Note that minor mean net stress $p^{net} = 1$ kPa was adopted instead of experimental $p^{net} = 0$ kPa, as the path "C" (which passed through the point of zero net stress and suction) could not be simulated otherwise. The hypoplastic model predicts zero stiffness for zero mean effective stress. The intergranular strain tensor was initialised to reflect one-dimensional compaction, as in the case of CDT simulations.

[Figure 13 about here.]

The available tests were adopted for calibration of the model parameters. Some parameters could not be calibrated using the available data, however. Those parameters had to be estimated and they do not influence substantially presented results of the simulations. Calibration of the parameters controlling G_{tp0} is detailed in Wong et al. [48]. A complete parameter set adopted in the simulations is in Table 3.

[Table 3 about here.]

Simulations of various portions of the tests are in Figs. 14 and 15. Using a single parameter set the model provides good predictions of various aspects of soil behaviour. In particular, the model predicts the dependency of wetting-induced collapse on mean net stress and suction (Figs. 14a, 14b and 15a). Thanks to the void-ratio dependent water retention curve it predicts correctly variation of S_r during constant suction tests (Figs. 14c,d) and constant mean net stress tests (Fig. 15b). The dependency of G_{tp0} on both mean net stress, suction and void ratio is also predicted properly (Figs. 14e,f and 15c).

[Figure 14 about here.]

[Figure 15 about here.]

5 Summary and conclusions

In the paper, we presented newly developed coupled hydro-mechanical hypoplastic model for partially saturated soils incorporating small strain stiffness. A number of features of the model were novel in comparison with earlier hypoplastic models. In particular, we adopted hysteretic void ratio dependent water retention curve. This required re-evaluation of a number of model components to ensure consistency of the model response with the void ratio, suction and suction history dependent position of the asymptotic state boundary surface and effective stress rate. The model was subsequently combined with the recently developed model for the dependency of the very small strain shear modulus on the effective stress, void ratio and suction. The small strain stiffness effects were incorporated using the intergranular strain concept by Niemunis and Herle [39], which was modified for unsaturated conditions. New features include suction-dependent size of the elastic range and an updated evolution equation for the intergranular strain, which reflects both the recent stress and suction histories.

The model was evaluated using two comprehensive experimental data sets. In the evaluation we focused on the small to very small strain stiffness predictions and hydro-mechanical coupling effects. Under various stress and suction histories, the model in most cases provided predictions qualitatively consistent with experimental data.

Acknowledgement

The research presented in this paper has been funded by the grant No. 14-32105S of the Czech Science Foundation.

Appendix

Summary of the proposed model mathematical formulation.

Definitions: Compact tensorial notation is used throughout. Second-order tensors are denoted with bold letters (e.g. $\boldsymbol{\sigma}$, $\mathbf{N}$) and fourth-order tensors with calligraphic bold letters (e.g. $\boldsymbol{\mathcal{L}}$, $\boldsymbol{\mathcal{A}}$). Symbols ”$\cdot$” and ”:” between tensors of various orders denote inner product with single and double contraction, respectively. $\|\dot{\boldsymbol{\epsilon}}\|$ represents the Euclidean norm of $\dot{\boldsymbol{\epsilon}}$. The trace operator is defined as $\operatorname{tr}\dot{\boldsymbol{\epsilon}} = \mathbf{1} : \dot{\boldsymbol{\epsilon}}$; $\mathbf{1}$ and $\boldsymbol{\mathcal{I}}$ denote second-order and fourth-order unity tensors, respectively. Following the sign convention of continuum mechanics, compression is taken as negative. However, mean stress $p = -\operatorname{tr}\boldsymbol{\sigma}/3$ and pore fluid and gas pressures u_w and u_a are defined to be positive in compression. The operator $\langle x \rangle$ denotes the positive part of any scalar function x, thus $\langle x\rangle = (x+|x|)/2$. The following variables are further adopted:

$$s = u_a - u_w \tag{48}$$

$$\boldsymbol{\sigma}^{net} = \boldsymbol{\sigma}^{tot} + u_a \tag{49}$$

where $\boldsymbol{\sigma}^{tot}$ is total Cauchy stress. The tensor products represented by "$\circ$" and "$\otimes$" are defined by

$$(\boldsymbol{p}\otimes\mathbf{1})_{ijkl} = p_{ij}1_{kl} \qquad (\boldsymbol{p}\circ\mathbf{1})_{ijkl} = \frac{1}{2}\left(p_{ik}1_{jl} + p_{il}1_{jk} + p_{jl}1_{ik} + p_{jk}1_{il}\right) \tag{50}$$

Parameters: φ_c, λ^*, κ^*, N, ν_{pp}, α_G, n_s, l_s, m, s_{en0}, e_0, λ_{p0}, a_e, A_g, n_g, m_g, k_g, R, β_r, χ_g, m_{rat}, r_m, $p_r = 1$ kPa.

State variables: $\boldsymbol{\sigma}^{net}$, s, S_r, e, a_{scan}, $\boldsymbol{\delta}$, s_{en}

Evolution equations for state variables:

$$\mathring{\boldsymbol{\sigma}}^{net} - \mathbf{1}\left(1-\gamma r_\lambda\right)\chi\dot{s} = \boldsymbol{\mathcal{M}}^{HM} : \dot{\boldsymbol{\epsilon}} + f_u\mathbf{H}_s \tag{51}$$

$$\dot{a}_{scan} = \frac{1-r_\lambda}{s_D(1-a_e)}\dot{s} \tag{52}$$

$$\dot{s}_{en} = -\frac{\gamma s_{en}}{e\lambda_{psu}}\dot{e} \tag{53}$$

$$\dot{e} = (1+e)\,\mathrm{tr}\,\dot{\boldsymbol{\epsilon}} \tag{54}$$

$$\mathring{\boldsymbol{\delta}} = \begin{cases} \left(\boldsymbol{\mathcal{I}} - \hat{\boldsymbol{\delta}}\otimes\hat{\boldsymbol{\delta}}\rho^{\beta_r}\right) : \dot{\boldsymbol{\epsilon}} - \boldsymbol{\delta}\frac{\langle -\dot{R}(s)\rangle}{R(s)} & \text{for } \hat{\boldsymbol{\delta}} : \dot{\boldsymbol{\epsilon}} > 0 \\ \dot{\boldsymbol{\epsilon}} & \text{for } \hat{\boldsymbol{\delta}} : \dot{\boldsymbol{\epsilon}} \leq 0 \end{cases} \tag{55}$$

$$\dot{R}(s) = r_m\left(r_\lambda\frac{\dot{s}}{s} + \frac{\gamma}{e\lambda_{psu}}\dot{e}\right) \tag{56}$$

$$S_r = \left(\frac{s_e}{s}\right)^{\lambda_p} \tag{57}$$

In the saturated case ($s < s_e$), Eqs. (51), (57) and (56) are replaced by

$$\mathring{\boldsymbol{\sigma}}^{net} - \mathbf{1}\dot{s} = \boldsymbol{\mathcal{M}}^{HM} : \dot{\boldsymbol{\epsilon}} \tag{58}$$

$$S_r = 1 \tag{59}$$

$$\dot{R}(s) = 0 \tag{60}$$

Formulation common to $S_r = 1$ and $S_r < 1$ states:

$$\boldsymbol{\mathcal{M}} = \left[\rho^{\chi_g} m_T + \left(1 - \rho^{\chi_g}\right) m_R\right] f_s \boldsymbol{\mathcal{L}} + \begin{cases} \rho^{\chi_g} \left(1 - m_T\right) f_s \boldsymbol{\mathcal{L}} : \hat{\boldsymbol{\delta}} \otimes \hat{\boldsymbol{\delta}} + \rho^{\chi_g} f_s f_d \mathbf{N} \hat{\boldsymbol{\delta}} & \text{for } \hat{\boldsymbol{\delta}} : \dot{\boldsymbol{\epsilon}} > 0 \\ \rho^{\chi_g} \left(m_R - m_T\right) f_s \boldsymbol{\mathcal{L}} : \hat{\boldsymbol{\delta}} \otimes \hat{\boldsymbol{\delta}} & \text{for } \hat{\boldsymbol{\delta}} : \dot{\boldsymbol{\epsilon}} \leq 0 \end{cases} \tag{61}$$

$$\rho = \frac{\|\boldsymbol{\delta}\|}{R(s)} \tag{62}$$

$$\hat{\boldsymbol{\delta}} = \begin{cases} \boldsymbol{\delta}/\|\boldsymbol{\delta}\| & \text{for } \boldsymbol{\delta} \neq \mathbf{0} \\ \mathbf{0} & \text{for } \boldsymbol{\delta} = \mathbf{0} \end{cases} \tag{63}$$

$$m_R = G_{tp0} \frac{4 A_m \alpha_G}{9 p \alpha_E} \left(\frac{\lambda^*_{act} \kappa^*}{\lambda^*_{act} + \kappa^*}\right) \frac{1}{1 - \nu_{pp} - 2 \frac{\alpha_E}{\alpha_\nu^2} \nu_{pp}^2} \tag{64}$$

$$m_T = m_R m_{rat} \tag{65}$$

$$\boldsymbol{\sigma} = \boldsymbol{\sigma}^{net} - \mathbf{1} \chi s \tag{66}$$

$$\gamma = 0.55 \tag{67}$$

$$s_e = s_{en} \left(a_e + a_{scan} - a_e a_{scan}\right) \tag{68}$$

$$s_D = \frac{s_{en}}{s_e} s \tag{69}$$

$$\lambda_p = \frac{\gamma}{\ln \chi_0} \ln \left[\left(\chi_0^{\frac{\lambda_{p0}}{\gamma}} - \chi_0\right) \left(\frac{e}{e_0}\right)^{(\gamma - 1)} + \chi_0\right] \tag{70}$$

$$\chi_0 = \left(\frac{s_{en0}}{s}\right)^{\gamma} \tag{71}$$

$$\lambda_{psu} = \frac{\gamma}{\ln \chi_{0su}} \ln \left[\left(\chi_{0su}^{\frac{\lambda_{p0}}{\gamma}} - \chi_{0su}\right) \left(\frac{e}{e_0}\right)^{(\gamma - 1)} + \chi_{0su}\right] \tag{72}$$

$$\chi_{0su} = \left(\frac{s_{en0}}{s_{en}}\right)^{\gamma} \tag{73}$$

$$\boldsymbol{\mathcal{L}} = \frac{1}{2} a_1 \mathbf{1} \circ \mathbf{1} + a_2 \mathbf{1} \otimes \mathbf{1} + a_3 \left(\boldsymbol{p} \otimes \mathbf{1} + \mathbf{1} \otimes \boldsymbol{p}\right) + a_4 \boldsymbol{p} \circ \mathbf{1} + a_5 \boldsymbol{p} \otimes \boldsymbol{p} \tag{74}$$

The tensor $\boldsymbol{p}$ is defined as $p_{ij} = n_i n_j$, where n_i is a unit vector normal to the plane of symmetry in transversely isotropic material.

$$a_1 = \alpha_E \left(1 - \nu_{pp} - 2\frac{\alpha_E}{\alpha_\nu^2}\nu_{pp}^2\right) \tag{75}$$

$$a_2 = \alpha_E \nu_{pp} \left(1 + \frac{\alpha_E}{\alpha_\nu^2}\nu_{pp}\right) \tag{76}$$

$$a_3 = \alpha_E \nu_{pp} \left(\frac{1}{\alpha_\nu} + \frac{\nu_{pp}}{\alpha_\nu} - 1 - \frac{\alpha_E}{\alpha_\nu^2}\nu_{pp}\right) \tag{77}$$

$$a_4 = \alpha_E \left(1 - \nu_{pp} - 2\frac{\alpha_E}{\alpha_\nu^2}\nu_{pp}^2\right) \frac{1 - \alpha_G}{\alpha_G} \tag{78}$$

$$a_5 = \alpha_E \left(1 - \frac{\alpha_E}{\alpha_\nu^2}\nu_{pp}^2\right) + 1 - \nu_{pp}^2 - 2\frac{\alpha_E}{\alpha_\nu}\nu_{pp}\left(1 + \nu_{pp}\right) - \frac{2\alpha_E}{\alpha_G}\left(1 - \nu_{pp} - 2\frac{\alpha_E}{\alpha_\nu^2}\nu_{pp}^2\right) \tag{79}$$

$$f_s = -\frac{3\,\mathrm{tr}\,\boldsymbol{\sigma}}{2A_m}\left(\frac{1}{\lambda_{act}^*} + \frac{1}{\kappa^*}\right) \tag{80}$$

$$A_m = \nu_{pp}^2\left(\frac{4\alpha_E}{\alpha_\nu} - 2\alpha_E^2 + 2\frac{\alpha_E^2}{\alpha_\nu^2} - 1\right) + \nu_{pp}\left(\frac{4\alpha_E}{\alpha_\nu} + 2\alpha_E\right) + 2\alpha_E + 1 \tag{81}$$

$$\alpha_E = \alpha_G^{(1/x_{GE})} \tag{82}$$

$$\alpha_\nu = \alpha_G^{(1/x_{G\nu})} \tag{83}$$

$$x_{GE} = 0.8 \tag{84}$$

$$x_{G\nu} = 1 \tag{85}$$

$$\mathbf{N} = -\frac{\boldsymbol{\mathcal{A}} : \boldsymbol{d}}{f_s f_d^A} \tag{86}$$

$$\boldsymbol{\mathcal{A}} = f_s \boldsymbol{\mathcal{L}} + \frac{\boldsymbol{\sigma}}{\lambda_{act}^*} \otimes \mathbf{1} \tag{87}$$

$$f_d = \left(\frac{2p}{p_e}\right)^{\alpha_f} \tag{88}$$

$$p_e = p_r \exp\left[\frac{N(s) - \ln(1+e)}{\lambda^*(s)}\right] \tag{89}$$

$$f_d^A = 2^{\alpha_f}(1 - F_m)^{\alpha_f/\omega} \tag{90}$$

$$F_m = \frac{9I_3 + I_1 I_2}{I_3 + I_1 I_2} \tag{91}$$

$$\omega = -\frac{\ln\left(\cos^2\varphi_c\right)}{\ln 2} + a\left(F_m - \sin^2\varphi_c\right) \tag{92}$$

$$a = 0.3 \tag{93}$$

$$I_1 = \mathrm{tr}\boldsymbol{\sigma} \tag{94}$$

$$I_2 = \frac{1}{2}\left[\boldsymbol{\sigma} : \boldsymbol{\sigma} - (I_1)^2\right] \tag{95}$$

$$I_3 = \det\boldsymbol{\sigma} \tag{96}$$

$$\boldsymbol{d} = \frac{\boldsymbol{d}^A}{\|\boldsymbol{d}^A\|} \tag{97}$$

$$\boldsymbol{d}^A = -\hat{\boldsymbol{\sigma}}^* + \mathbf{1}\left[\frac{2}{3} - \frac{\cos 3\theta + 1}{4}F_m^{1/4}\right]\frac{F_m^{\xi/2} - \sin^\xi\varphi_c}{1 - \sin^\xi\varphi_c} \tag{98}$$

$$\cos 3\theta = -\sqrt{6}\frac{\mathrm{tr}\left(\hat{\boldsymbol{\sigma}}^* \cdot \hat{\boldsymbol{\sigma}}^* \cdot \hat{\boldsymbol{\sigma}}^*\right)}{\left[\hat{\boldsymbol{\sigma}}^* : \hat{\boldsymbol{\sigma}}^*\right]^{3/2}} \tag{99}$$

$$\xi = 1.7 + 3.9\sin^2\varphi_c \tag{100}$$

$$\hat{\boldsymbol{\sigma}}^* = \frac{\boldsymbol{\sigma}}{\mathrm{tr}\,\boldsymbol{\sigma}} - \frac{\mathbf{1}}{3} \tag{101}$$

$$\alpha_f = \frac{\ln\left[\frac{\lambda^* - \kappa^*}{\lambda^* + \kappa^*}\left(\frac{3 + a_f^2}{a_f\sqrt{3}}\right)\right]}{\ln 2} \tag{102}$$

$$a_f = \frac{\sqrt{3}\left(3 - \sin\varphi_c\right)}{2\sqrt{2}\sin\varphi_c} \tag{103}$$

$$\mathbf{H}_s = -\frac{c_i r_\lambda \boldsymbol{\sigma}}{s\lambda^*(s)}\left(n_s - l_s \ln\frac{p_e}{p_r}\right)\langle -\dot{s}\rangle \tag{104}$$

$$c_i = \frac{\left(\lambda^*_{act} + \kappa^*\right)\left(2^{\alpha_f} - f_d\right) + 2\kappa^* f_d}{\left(\lambda^*_{act} + \kappa^*\right)\left(2^{\alpha_f} - f_d^A\right) + 2\kappa^* f_d^A} \tag{105}$$

$$f_u = \left(\frac{f_d}{f_d^A}\right)^{\left(m/\alpha_f\right)} \tag{106}$$

Formulations specific to $S_r < 1$ states:

$$\boldsymbol{\mathcal{M}}^{HM} = \boldsymbol{\mathcal{M}} - \frac{s(1+e)\gamma^2}{e\lambda_{psu}}\left(\frac{s_{en}}{s}\right)^\gamma \mathbf{1} \otimes \mathbf{1} \tag{107}$$

$$R(s) = R + r_m \ln \frac{s}{s_e} \tag{108}$$

$$G_{tp0} = p_r A_g \left(\frac{p}{p_r}\right)^{n_g} e^{(-m_g)} \left(\frac{s}{s_e}\right)^{k_g} \tag{109}$$

$$\chi = \left(\frac{s_e}{s}\right)^{\gamma} \tag{110}$$

$$r_\lambda = \begin{cases} 1 & \text{for} \quad s = s_D \quad \text{and} \quad \dot{s} > 0 \\ 1 & \text{for} \quad s = a_e s_D \quad \text{and} \quad \dot{s} < 0 \\ \frac{\lambda_{pscan}}{\lambda_p} & \text{otherwise} \end{cases} \tag{111}$$

$$\lambda^*_{act} = \lambda^*(s) \frac{e\lambda_{psu}}{e\lambda_{psu} - \gamma(1+e)[n_s - l_s \ln(p/p_r)]} \tag{112}$$

$$N(s) = N + n_s \ln \left(\frac{s}{s_e}\right) \qquad \lambda^*(s) = \lambda^* + l_s \ln \left(\frac{s}{s_e}\right) \tag{113}$$

Alternative formulations specific to $S_r = 1$ states:

$$\boldsymbol{\mathcal{M}}^{HM} = \boldsymbol{\mathcal{M}} \tag{114}$$

$$R(s) = R \tag{115}$$

$$G_{tp0} = p_r A_g \left(\frac{p}{p_r}\right)^{n_g} e^{(-m_g)} \tag{116}$$

$$\chi = 1 \tag{117}$$

$$r_\lambda = 1 \tag{118}$$

$$\lambda^*_{act} = \lambda^*(s) = \lambda^* \tag{119}$$

$$N(s) = N \tag{120}$$

References

[1] E. E. Alonso, J.-M. Pereira, J. Vaunat, and S. Olivella. A microstructurally based effective stress for unsaturated soils. *Géotechnique*, 60(12):913–925, 2010.

[2] M. Biglari, A. d'Onofrio, C. Mancuso, M. K. Jafari, A. Shafiee, and I. Ashayeri. Small-strain stiffness of Zenoz kaolin in unsaturated conditions. *Canadian Geotechnical Journal*, 49:311–322, 2012.

[3] M. Biglari, C. Mancuso, A. d'Onofrio, M. K. Jafari, and A. Shafiee. Modelling the initial shear stiffness of unsaturated soils as a function of the coupled effects of the void ratio and the degree of saturation. *Computers and Geotechnics*, 38:709–720, 2011.

[4] A. W. Bishop. The principle of effective stress. *Teknisk Ukeblad*, 106(39):859–863, 1959.

[5] R. Brooks and A. Corey. Hydraulic properties of porous media. *Hydrology paper No. 3, Colorado state University*, 1964.

[6] R. Butterfield. A natural compression law for soils. *Géotechnique*, 29(4):469–480, 1979.

[7] O. Coussy. Revisiting the constitutive equations of unsaturated porous solids using a Lagrangian saturation concept. *International Journal for Numerical and Analytical Methods in Geomechanics*, 31(15):1675–1694, 2007.

[8] G. Della Vecchia, C. Jommi, and E. Romero. A fully coupled elastic-plastic hydromechanical model for compacted soils accounting for clay activity. *International Journal for Numerical and Analytical Methods in Geomechanics*, 37:503–535, 2013.

[9] F. D'Onza, D. Gallipoli, S. Wheeler, F. Casini, J. Vaunat, N. Khalili, L. Laloui, C. Mancuso, D. Mašín, M. Nuth, M. Pereira, and R. Vassallo. Benchmark of constitutive models for unsaturated soils. *Géotechnique*, 61(4):283–302, 2011.

[10] K. C. Ellison, K. Soga, and B. Simpson. A strain space soil model with evolving stiffness anisotropy. *Géotechnique*, 62(7):627–641, 2012.

[11] W. Fuentes and T. Triantafyllidis. Hydro-mechanical hypoplastic models for unsaturated soils under isotropic stress conditions. *Computers and Geotechnics*, 51:72–82, 2013.

[12] D. Gallipoli, A. Gens, R. Sharma, and J. Vaunat. An elasto-plastic model for unsaturated soil incorporating the effects of suction and degree of saturation on mechanical behaviour. *Géotechnique*, 53(1):123–135, 2003.

[13] H. Ghasemzadeh and S. A. Ghoreishian Amiri. A hydro-mechanical elastoplastic model for unsaturated soils under isotropic loading conditions. *Computers and Geotechnics*, 51:91–100, 2013.

[14] W. G. Gray, B. A. Schrefler, and F. Pesavento. The solid phase stress tensor in porous media mechanics and the Hill-Mandel condition. *Journal of the Mechanics and Physics of Solids*, 57:539–554, 2009.

[15] G. Gudehus and D. Mašín. Graphical representation of constitutive equations. *Géotechnique*, 59(2):147–151, 2009.

[16] N. Khalili, M. A. Habte, and S. Valliapan. A bounding surface plasticity model for cyclic loading of granular soils. *International Journal for Numerical Methods in Engineering*, 63:1939–1960, 2005.

[17] N. Khalili, M. A. Habte, and S. Zargarbashi. A fully coupled flow-deformation model for cyclic analysis of unsaturated soils including hydraulic and mechanical hystereses. *Computers and Geotechnics*, 35(6):872–889, 2008.

[18] N. Khalili and M. H. Khabbaz. A unique relationship for χ for the determination of the shear strength of unsaturated soils. *Géotechnique*, 48(2):1–7, 1998.

[19] N. Khalili and S. Zargarbashi. Influence of hydraulic hysteresis on effective stress in unsaturated soils. *Géotechnique*, 60(9):729–734, 2010.

[20] A. Khosravi and J. S. McCartney. Impact of hydraulic hysteresis on the small strain shear modulus of low plasticity soils. *Journal of Geotechnical and Geoenvironmental Engineering ASCE*, 138(11):1326–1333, 2012.

[21] X. S. Li. Modelling of hysteresis response for arbitrary wetting/drying paths. *Computers and Geotechnics*, 32:133–137, 2005.

[22] C. Liu and K. Muraleetharan. Coupled hydro-mechanical elastoplastic constitutive model for unsaturated sands and silts. I: Formulation. *International Journal of Geomechanics*, 12(3):239–247, 2012.

[23] M. Lloret-Cabot, M. Sánchez, and S. J. Wheeler. Formulation of a three-dimensional constitutive model for unsaturated soils incorporating mechanical-water retention couplings. *International Journal for Numerical and Analytical Methods in Geomechanics*, 37(17):3008–3035, 2013.

[24] M. Lloret-Cabot, S. J. Wheeler, and M. Sánchez. Unification of plastic compression in a coupled mechanical and water retention model for unsaturated soils. *Canadian Geotechnical Journal (in print, DOI:10.1139/cgj-2013-0360)*, 2014.

[25] D. Mašín. Predicting the dependency of a degree of saturation on void ratio and suction using effective stress principle for unsaturated soils. *International Journal for Numerical and Analytical Methods in Geomechanics*, 34:73–90, 2010.

[26] D. Mašín. Asymptotic behaviour of granular materials. *Granular Matter*, 14(6):759–774, 2012.

[27] D. Mašín. Hypoplastic Cam-clay model. *Géotechnique*, 62(6):549–553, 2012.

[28] D. Mašín. Clay hypoplasticity with explicitly defined asymptotic states. *Acta Geotechnica*, 8(5):481–496, 2013.

[29] D. Mašín. Double structure hydromechanical coupling formalism and a model for unsaturated expansive clays. *Engineering Geology*, 165:73–88, 2013.

[30] D. Mašín. Clay hypoplasticity model including stiffness anisotropy. *Géotechnique*, 64(3):232–238, 2014.

[31] D. Mašín and N. Khalili. A hypoplastic model for mechanical response of unsaturated soils. *International Journal for Numerical and Analytical Methods in Geomechanics*, 32(15):1903–1926, 2008.

[32] D. Mašín and N. Khalili. A thermo-mechanical model for variably saturated soils based on hypoplasticity. *International Journal for Numerical and Analytical Methods in Geomechanics (in print, DOI: 10.1002/nag.1058)*, 2011.

[33] D. Mašín and J. Rott. Small strain stiffness anisotropy of natural sedimentary clays: review and a model. *Acta Geotechnica*, 9(2):299–312, 2014.

[34] K. K. Muraleetharan, C. Liu, C. Wei, T. C. G. Kibbey, and L. Chen. An elastoplatic framework for coupling hydraulic and mechanical behavior of unsaturated soils. 25(3):473–490, 2009.

[35] C. W. W. Ng and J. Xu. Effects of current suction ratio and recent suction history on small-strain behaviour of an unsaturated soil. *Canadian Geotechnical Journal*, 49:226–243, 2012.

[36] C. W. W. Ng, J. Xu, and S. Y. Yung. Effects of wetting-drying and stress ratio on anisotropic stiffness of an unsaturated soil at very small strains. *Canadian Geotechnical Journal*, 46:1062–1076, 2009.

[37] C. W. W. Ng and S. Y. Yung. Determination of the anisotropic shear stiffness of an unsaturated decomposed soil. *Géotechnique*, 58(1):23–35, 2008.

[38] A. Niemunis, C. E. Grandas Tavera, and L. F. Prada Sarmiento. Anisotropic visco-hypoplasticity. *Acta Geotechnica*, 4(4):293–314, 2009.

[39] A. Niemunis and I. Herle. Hypoplastic model for cohesionless soils with elastic strain range. *Mechanics of Cohesive-Frictional Materials*, 2(4):279–299, 1997.

[40] M. Nuth and L. Laloui. Advances in modelling hysteretic water retention curve in deformable soils. *Computers and Geotechnics*, 35(6):835–844, 2008.

[41] D. M. Pedroso, D. Sheng, and J. Zhao. The concept of reference curves for constitutive modelling in soil mechanics. *Computers and Geotechnics*, 36:149–165, 2009.

[42] A. Sawangsuriya, T. B. Edil, and P. J. Bosscher. Modulus-suction-moisture relationship for compacted soils in postcompaction state. *Journal of Geotechnical and Geoenvironmental Engineering ASCE*, 135(10):1390–1403, 2009.

[43] S. S. Sharma and M. Fahey. Deformation characteristics of two cemented calcareous soils. *Canadian Geotechnical Journal*, 41:1139–1151, 2004.

[44] S. E. Stallebrass and R. N. Taylor. Prediction of ground movements in overconsolidated clay. *Géotechnique*, 47(2):235–253, 1997.

[45] R. Vasallo, C. Mancuso, and F. Vinale. Effects of net stress and suction history on the small strain stiffness of a compacted clayey silt. *Canadian Geotechnical Journal*, 44(4):447–462, 2007.

[46] S. J. Wheeler, A. Näätänen, M. Karstunen, and M. Lojander. An anisotropic elastoplastic model for soft clays. *Canadian Geotechnical Journal*, 40:403–418, 2003.

[47] S. J. Wheeler, R. S. Sharma, and M. S. R. Buisson. Coupling of hydraulic hysteresis and stress-strain behaviour in unsaturated soils. *Géotechnique*, 53:41–54, 2003.

[48] K. S. Wong, D. Mašín, and C. W. W. Ng. Modelling of shear stiffness of unsaturated fine grained soils at very small strains. *Computers and Geotechnics*, 56:28–39, 2014.

[49] J. Xu. *Experimental study of effects of suction history and wetting-drying on small strain stiffness of an unsaturated soil*. PhD thesis, The Hong Kong University of Science and Technology, 2011.

[50] A.-N. Zhou, D. Sheng, S. W. Sloan, and A. Gens. Interpretation of unsaturated soil behaviour in the stress - Saturation space, I: Volume change and water retention behaviour. *Computers and Geotechnics*, 43:178–187, 2012.

[51] C. Zhou. *Constitutive modelling and experimental study of cyclic behaviour of unsaturated soil at different temperatures*. PhD thesis, The Hong Kong University of Science and Technology (in preparation), 2014.

[52] M. Zytynski, M. F. Randolph, and R. Nova. On modelling the unloading-reloading behaviour of soils. *International Journal for Numerical and Analytical Methods in Geomechanics*, 2(1):87–93, 1978.

List of Figures

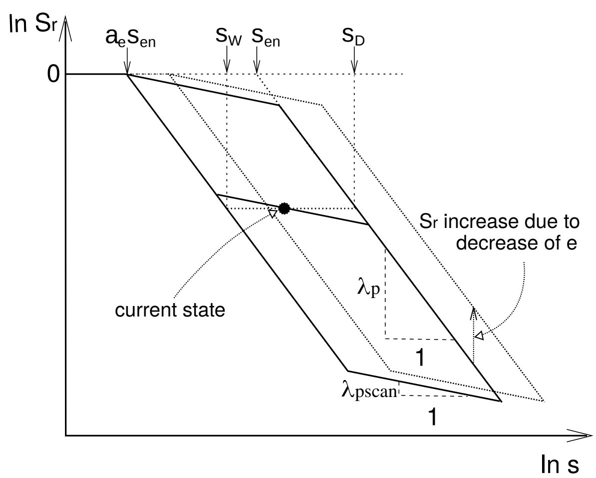

Figure 1: Hysteretic water retention curve adopted in the proposed model.

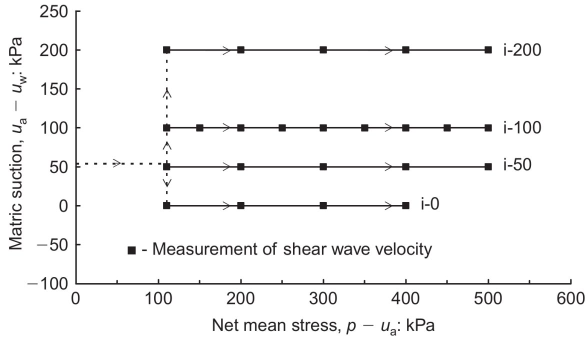

(a)

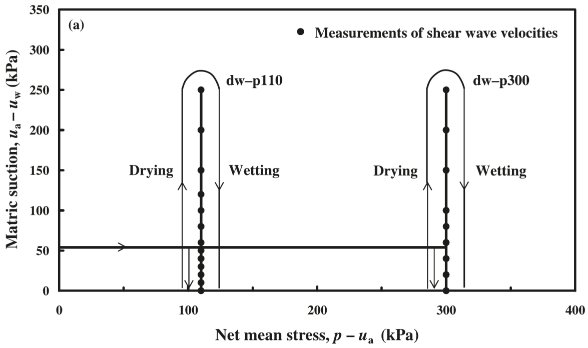

(b)

Figure 2: (a) Stress-suction paths of simulated isotropic compression tests [37]; (b) Stress-suction paths of simulated wetting-drying tests [36].

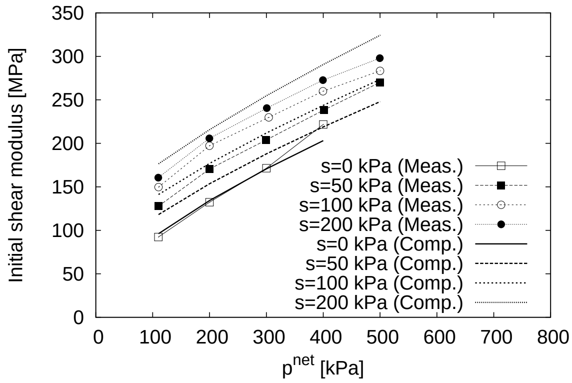

Figure 3: G_{tp0} dependency on mean net stress during constant suction isotropic compression tests, experimental data by Ng and Yung [37] and model simulations.

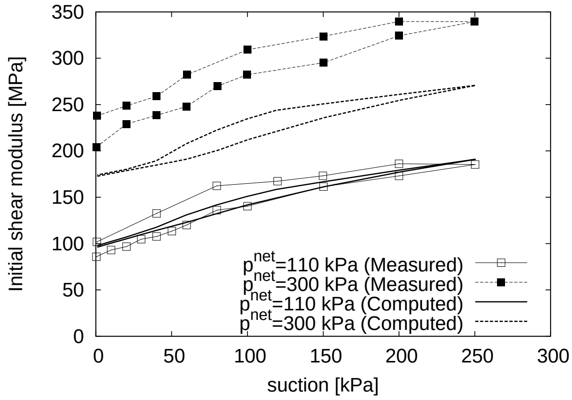

Figure 4: G_{tp0} dependency on suction during constant mean net stress wetting-drying tests. Experimental data by Ng et al. [36] and model simulations.

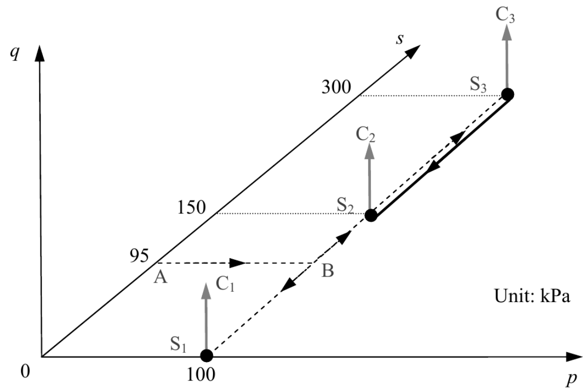

Figure 5: Stress-suction histories adopted in small strain stiffness tests (from Xu, 2011).

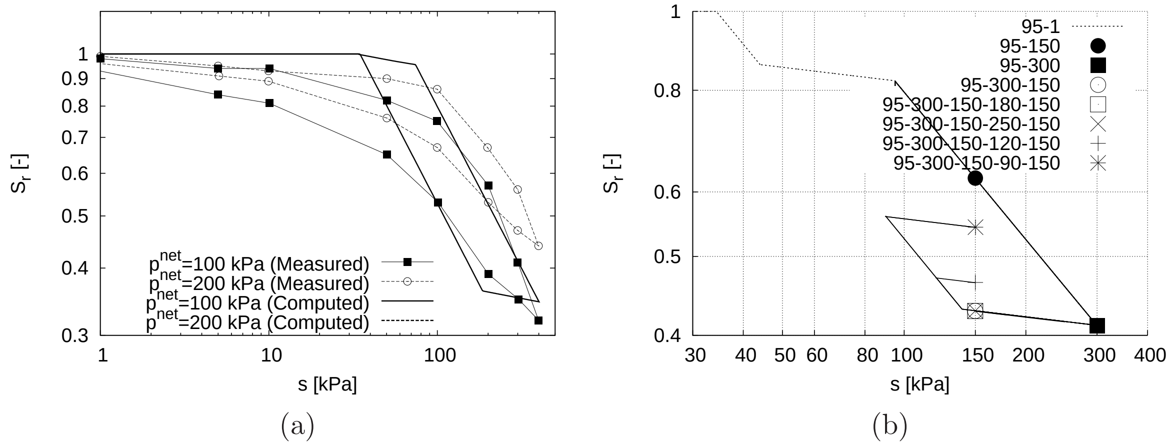

Figure 6: Hysteretic water retention curve. (a) Experimental data by Ng and Xu (2012) and model predictions. (b) Suction vs S_r histories and initial hydraulic states of the simulated shear tests.

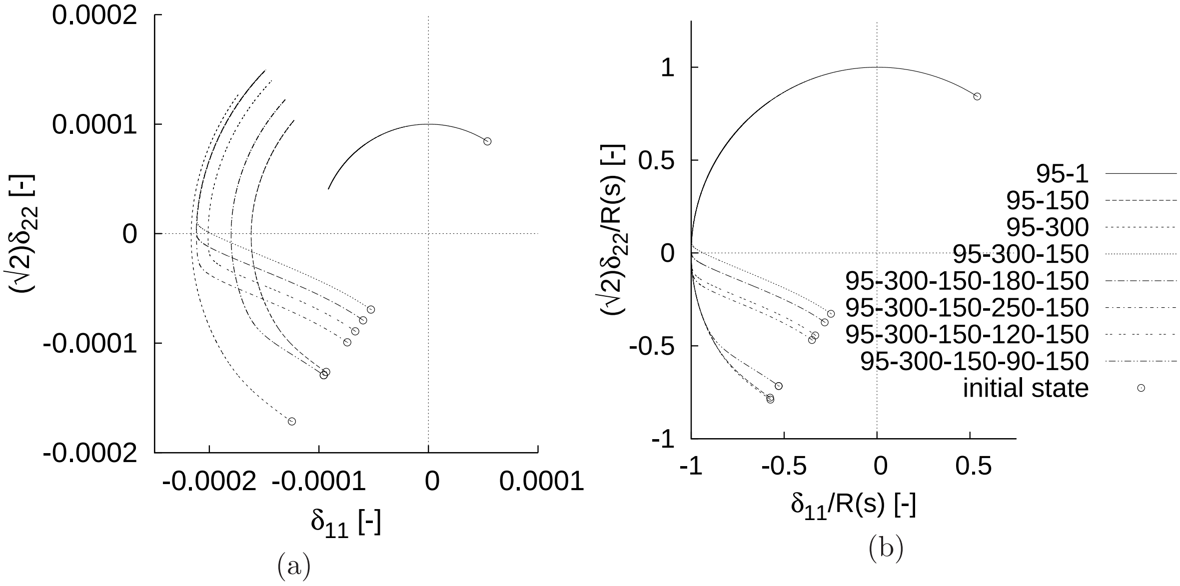

Figure 7: Intergranular strain evolution during the shear phase in different tests at $p^{net} =$ 100 kPa. (a) vertical (δ_{11}) and horisontal (δ_{22}) components of the intergranular strain; (b) intergranular strain normalised by $R(s)$. $95-300-150-50-150$ is identical to $95-300-150-90-150$ and not shown for clarity.

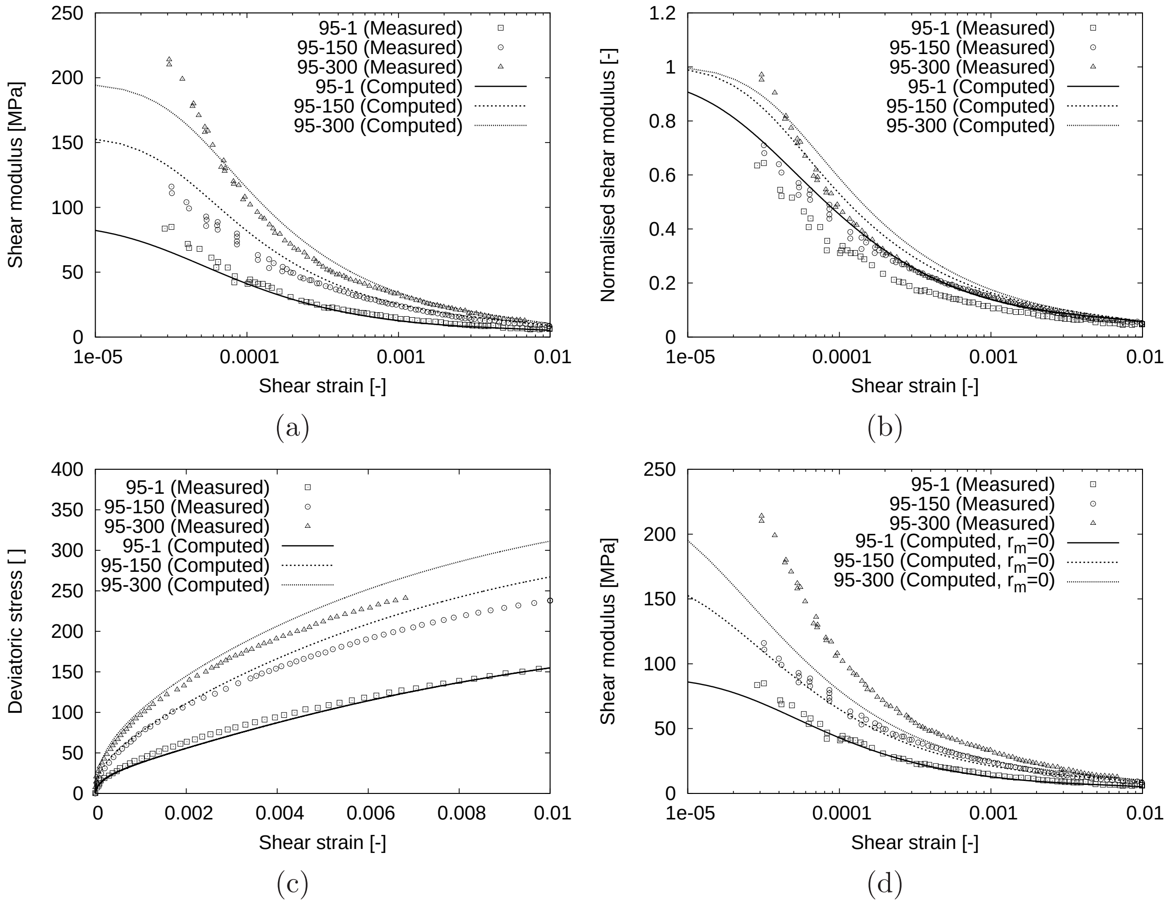

Figure 8: Stiffness degradation curves from the first set of experiments, experimental data by Ng and Xu (2012) compared with the model predictions. (a) G vs. shear strain curve, (b) G/G_{tp0} vs. shear strain curve, (c) deviatoric stress vs. shear strain curve, (d) G vs. shear strain curve predicted by the model with $r_m = 0$.

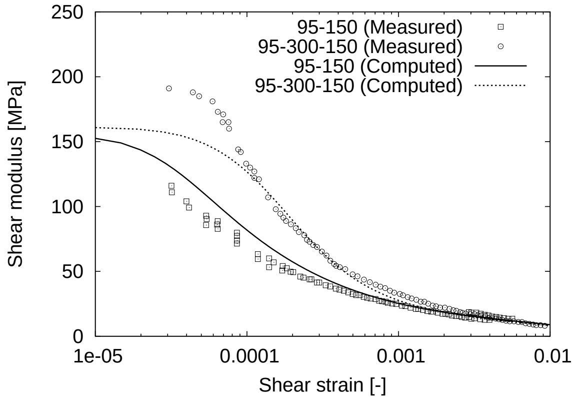

(a)

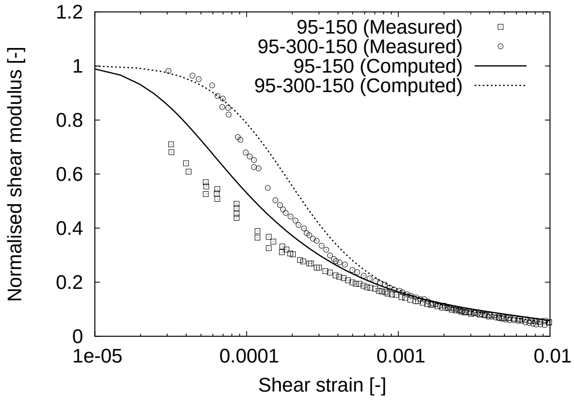

(b)

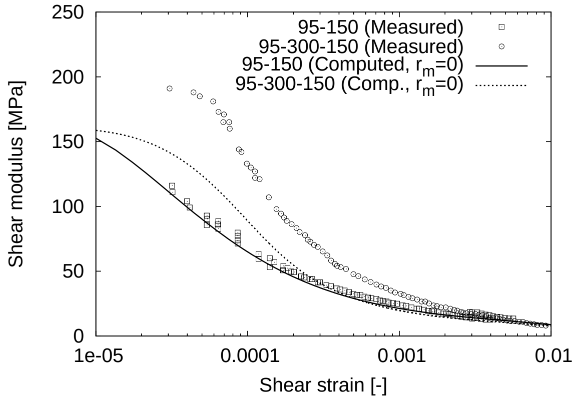

(c)

Figure 9: Simulations of the second set of experiments. (a) Stiffness degradation curves, (b) G/G_{tp0} vs. shear strain curves, (c) predictions with $r_m = 0$. Experimental data by Ng and Xu (2012) compared with the model predictions.

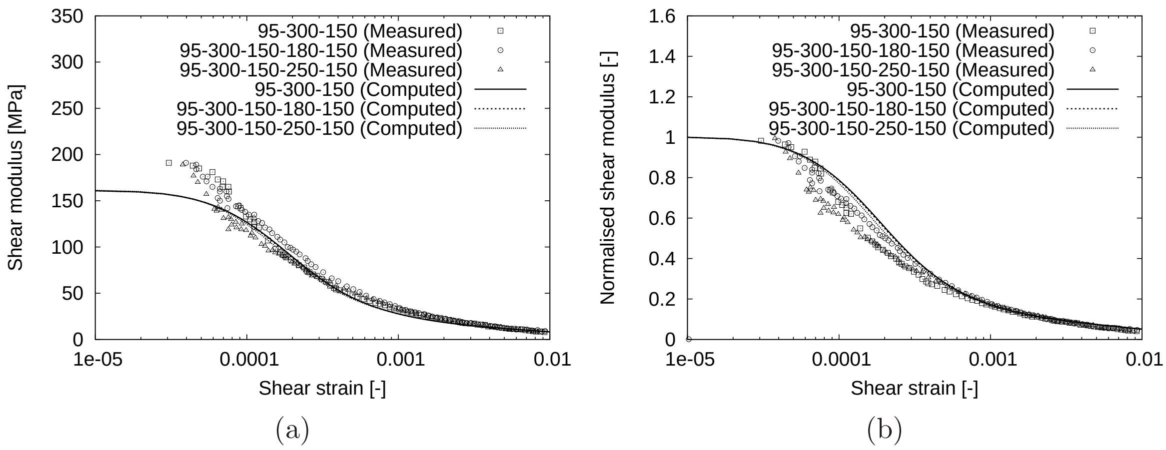

Figure 10: Simulations of the third set of experiments. (a) Stiffness degradation curves, (b) G/G_{tp0} vs. shear strain curves. Experimental data by Ng and Xu (2012) compared with the model predictions.

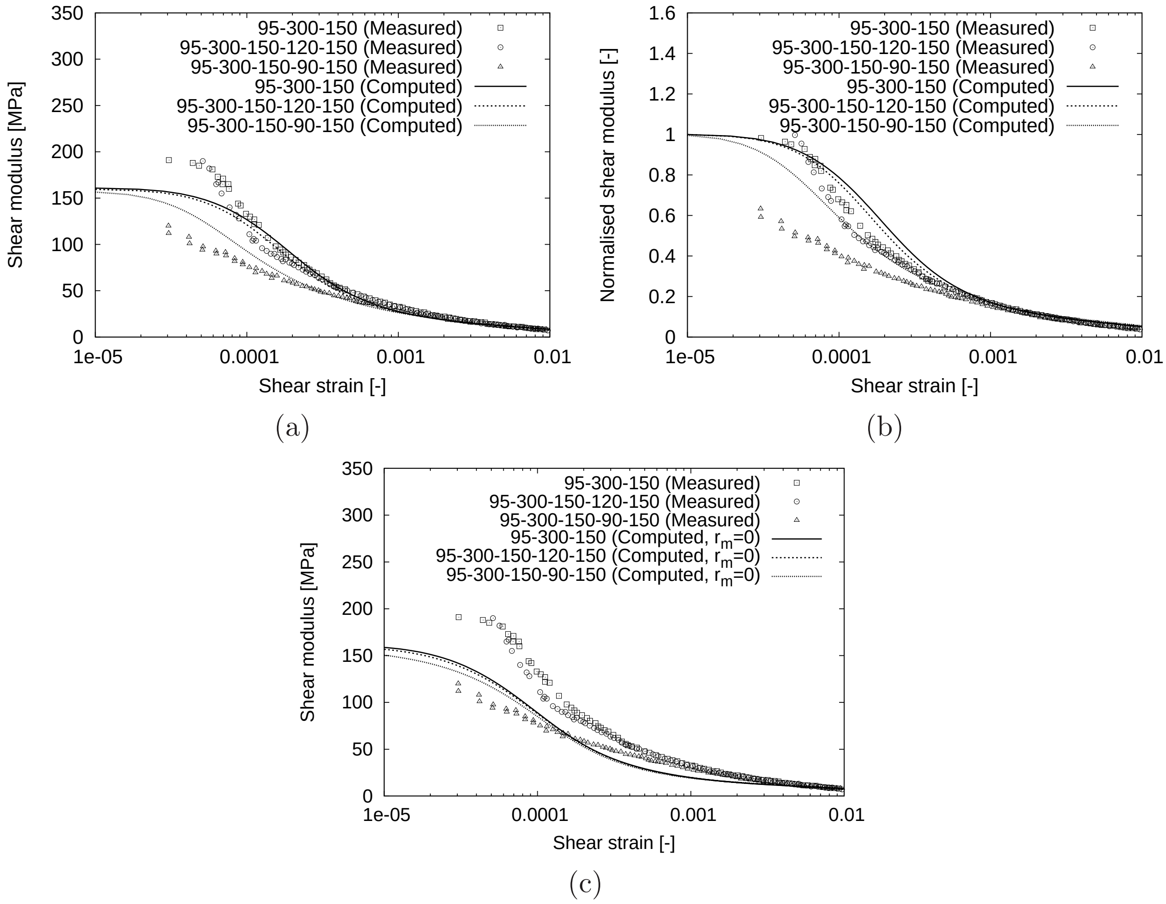

Figure 11: Simulations of the fourth set of experiments. (a) Stiffness degradation curves, (b) G/G_{tp0} vs. shear strain curves, (c) stiffness degradation curves simulated with $r_m = 0$. Experimental data by Ng and Xu (2012) compared with the model predictions.

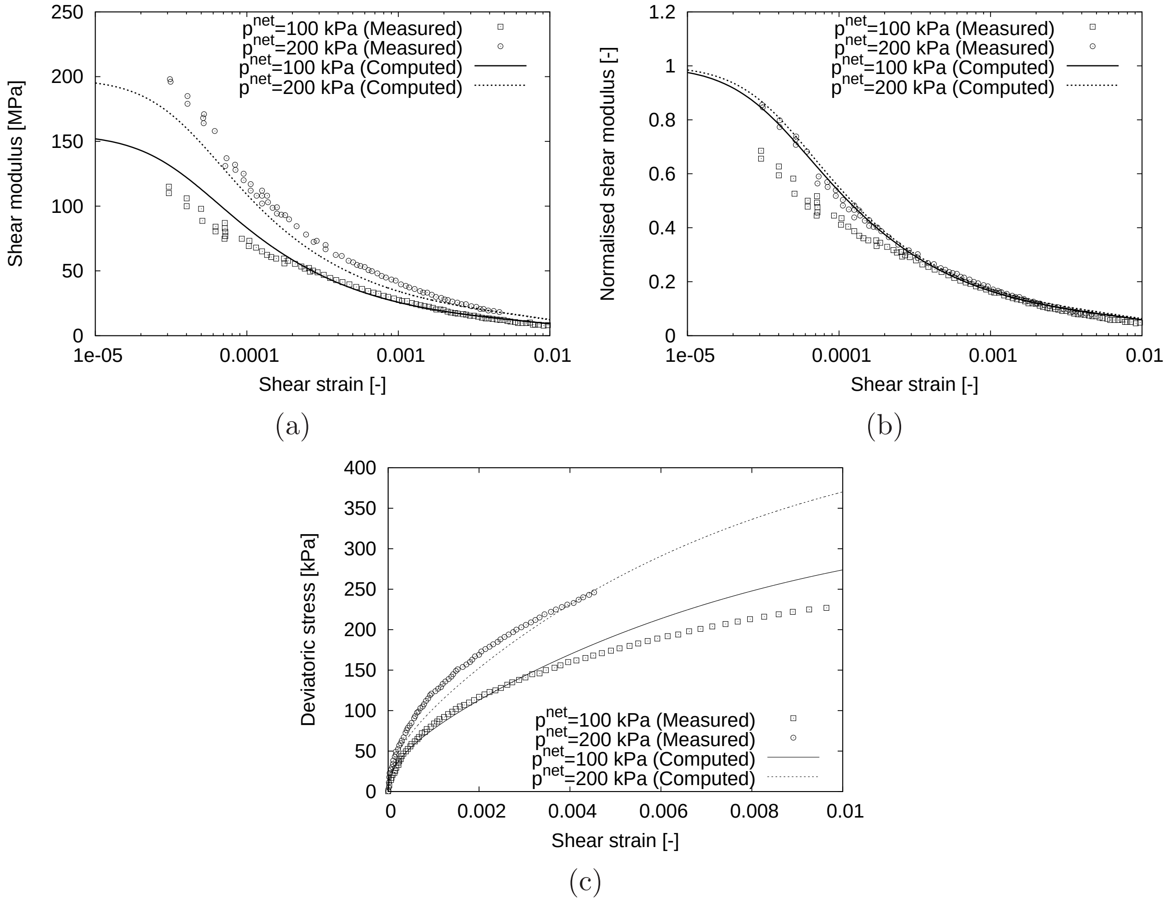

Figure 12: Simulations of the fifth set of experiments, experimental data by Ng and Xu (2012) compared with the model predictions. (a) G vs. shear strain curve, (b) G/G_{tp0} vs. shear strain curve, (c) deviatoric stress vs. shear strain curve

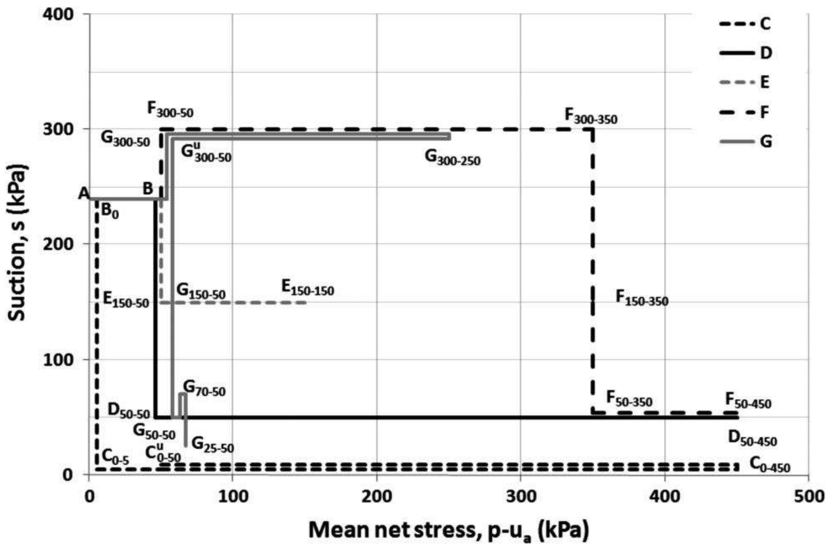

Figure 13: Experimental programme on Zenos Kaolin (Biglari et al., 2012).

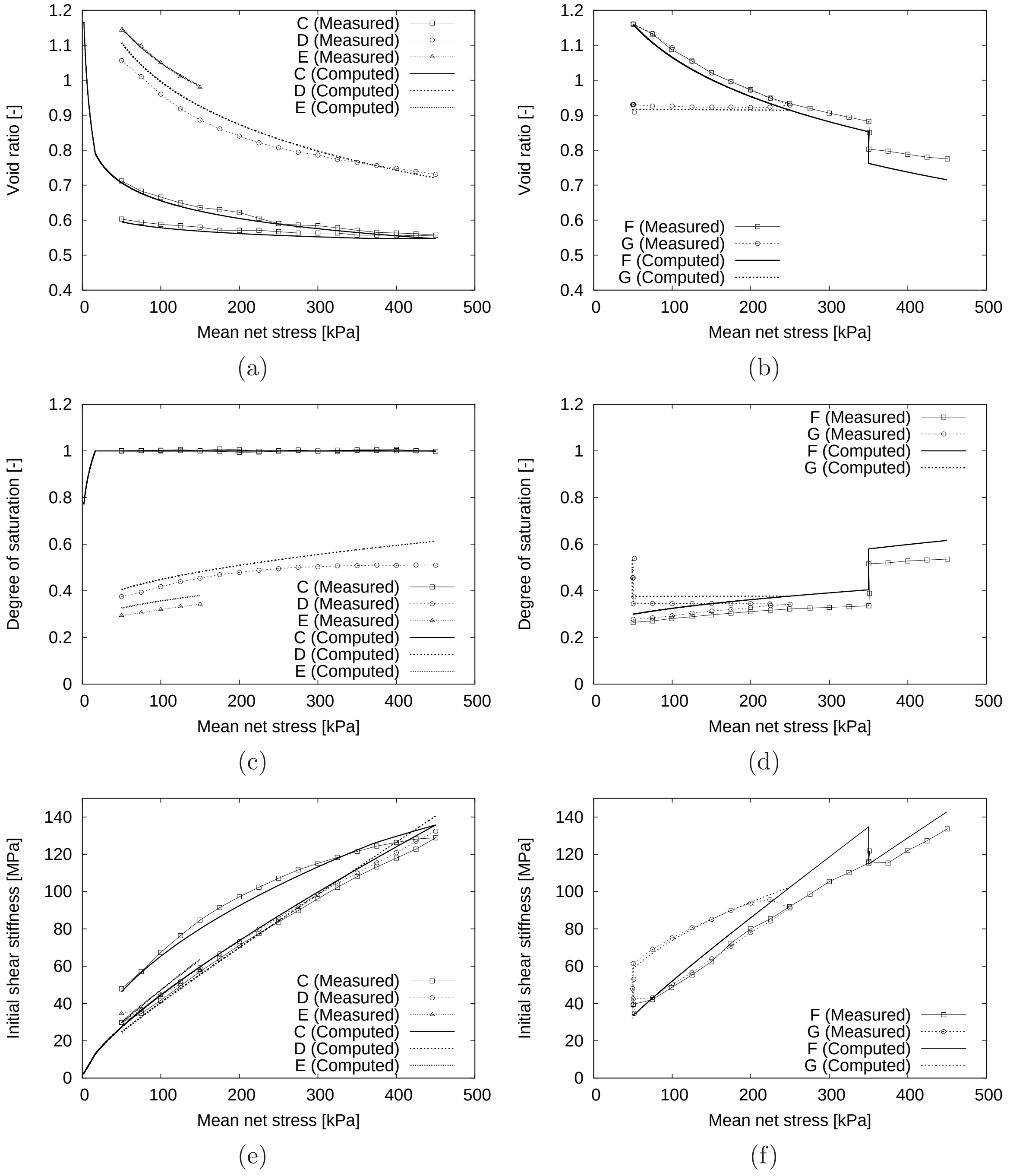

Figure 14: Simulations of Zenos Kaolin experiments, constant suction paths. Experimental data by Biglari et al. (2012).

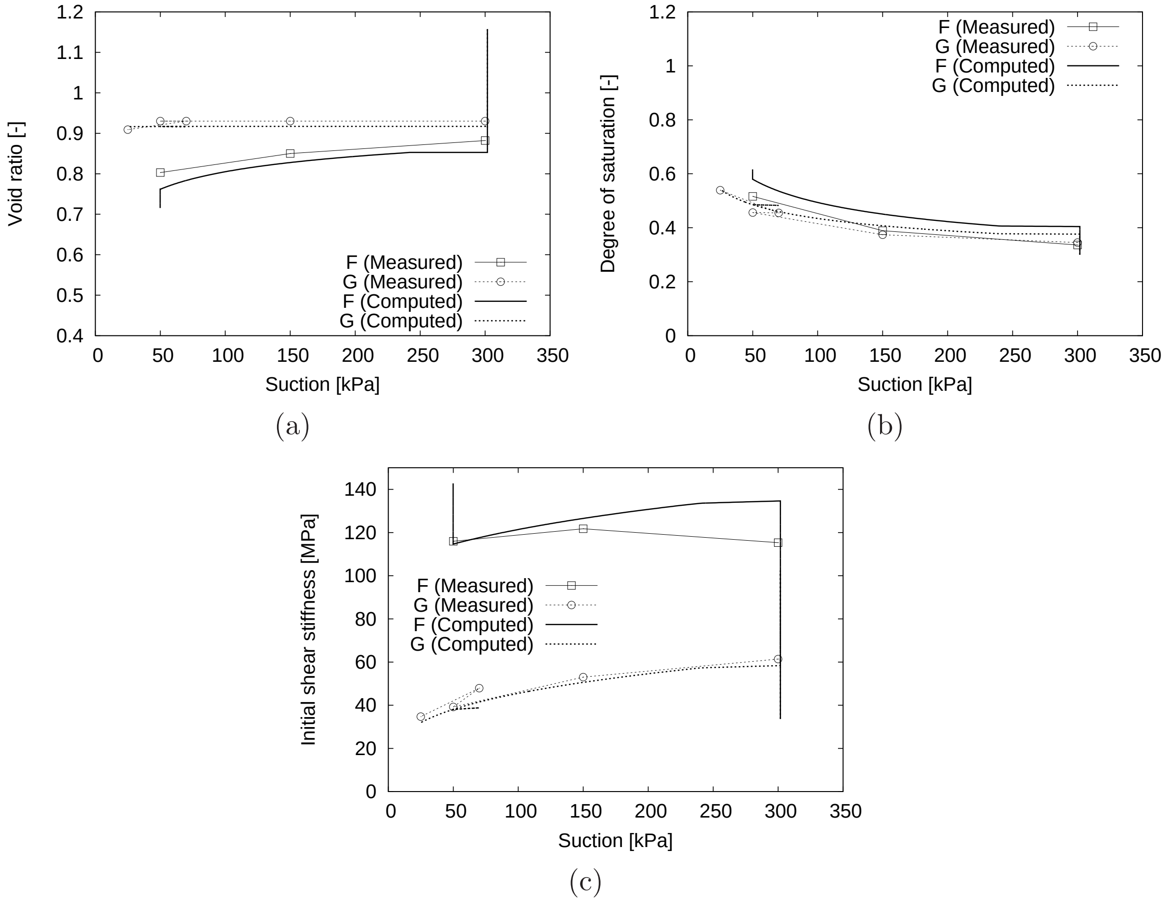

Figure 15: Simulations of Zenos Kaolin experiments, constant p^{net} paths. Experimental data by Biglari et al. (2012).

List of Tables

Table 1: Parameters of the proposed model with literature sources describing calibration procedures for individual parameters.

model parameter	description of the partial model	literature source
φ_c, λ^*, κ^*, N, ν_{pp}	Hypoplastic model for saturated soils with explicit asymptotic state boundary surface formulation	Mašín [28]
α_G	Model for the very small strain stiffness anisotropy of sedimentary clays	Mašín and Rott [33]
n_s, l_s, m	Mechanical model for partially saturated soils	Mašín and Khalili [31]
s_{en0}, e_0, λ_{p0}	Void ratio dependent non-hysteretic water retention model	Mašín [25]
a_e	Parameter specifying hydraulic hysteresis (ratio of air expulsion and air entry values of suction)	this paper
A_g, n_g, m_g, k_g	Model for very small strain stiffness of partially saturated soils	Wong et al. [48]
R, β_r, χ_g	Intergranular strain concept for small strain stiffness of saturated soils	Niemunis and Herle [39]
m_{rat}	Ratio of m_T/m_R of the intergranular strain model	Niemunis and Herle [39] and this paper, Eq. (41)
r_m	Parameter controlling suction-dependent size of the elastic range	this paper, Eq. (42)
γ	Parameter of the effective stress model, a default value of $\gamma = 0.55$ suggested in [18]	Khalili and Khabbaz [18]

Table 2: CDT parameters of the proposed model adopted in all simulations.

basic model	φ_c	λ^*	κ^*	N	ν_{pp}	α_G
	$35°$	0.053	0.005	0.76	0.25	1
unsat.	n_s	l_s	m			
mechanical	0	0	(n/r)			
WRC model	s_{en0}	e_0	λ_{p0}	a_e		
	67 kPa	0.568	0.6	0.5		
G_{tp0} model	A_g	n_g	m_g	k_g		
	4220	0.55	0.9	0.2		
intergr. strain	R	β_r	χ_g	m_{rat}	r_m	
model	10^{-4}	2	1	1	8x10^{-5}	

Table 3: Zenos Kaolin parameters of the proposed model adopted in all simulations.

basic model	φ_c	λ^*	κ^*	N	ν_{pp}	α_G
	33°	0.0466	0.0143	0.725	0.25	1
unsat.	n_s	l_s	m			
mechanical	0.11	0.012	1			
WRC model	s_{en0}	e_0	λ_{p0}	a_e		
	1 kPa	0.93	0.16	0.5		
G_{tp0} model	A_g	n_g	m_g	k_g		
	2176	0.375	3.05	0.243		
intergr. strain	R	β_r	χ_g	m_{rat}	r_m	
model	10^{-4}	2	1	1	15x10^{-5}	